Texas A&M University
Mechanical Engineering Department
Turbomachinery laboratory

Identification of Force Coefficients in a Squeeze Film Damper with a Mechanical Seal

Research progress Report to the Turbomachinery Research Consortium
By

TRC-SFD-1-05

Adolfo Delgado

Research Assistant

Luis San Andrés

Professor

May 2005

TRC Project 32513/1519C3
Experimental Force Coefficients for a Sealed Squeeze Film Damper

Executive Summary

Squeeze film dampers (SFDs) with low levels of external pressurization and poor end sealing are prone to air entrapment, thus not generating enough damping capability. Predictive models are too restrictive and do very poorly. Single frequency, unidirectional load experiments were conducted on a recently completed sealed SFD test rig. The damper journal is 1" in length and 5" in diameter, with nominal clearance of 5 mils (0.127 mm). The SFD feed end is flooded with oil, while the exit end contains a recirculation groove and four orifice discharge ports to prevent air ingestion. The end is fully sealed with a wave-spring that pushes a seal ring into contact with the SFD journal. The measurements conducted without and with lubricant in the squeeze film lands, along with a frequency domain identification procedure, render the mechanical seal dry-friction force and viscous damping force coefficients as functions of frequency and motion amplitude. The end seal arrangement is quite effective in eliminating side leakage and preventing air entrainment into the film lands. Importantly enough, the dry friction force, arising from the contact forces in relative motion, increases significantly the test element equivalent viscous damping coefficients. The identified system damping coefficients are thus frequency and amplitude of motion dependent, albeit decreasing rapidly as the motion parameters increase. Identified force coefficients, damping and added mass, for the squeeze film damper alone agree very well with predictions based on the full film classical lubrication model

Table of Contents

List of Tables

List of Figures

Nomenclature

c	Bearing radial clearance [m]
$C_{rv} = C_s$	Structure residual damping coefficient [N.s/m]
C_{seal}	$(4/\pi)\ F_\mu/[\omega\|z\|]$ equivalent viscous damping for mechanical seal [N.s/m]
$C_{\alpha\beta}$	Identified squeeze film damping coefficients [N.s/m], $\alpha, \beta = x,y$
$C_{t\alpha}$	$C_{t\alpha}=C_{rv}+C_{seal}+C_{\alpha\alpha}$, System damping coefficients [N.s/m], $\alpha=x,y$
$D_{\alpha\beta}$	Identified squeeze film added mass coefficients [kg], $\alpha, \beta = x,y$
E	Energy dissipated [J]
$F_{x,y}$	External (shaker) forces applied to bearing [N]
$\bar{F}_{x,y}$	Frequency components of external forces applied to bearing [N]
F_μ	Dry friction force from contact in mechanical seal [N]
f_n	Natural frequency [Hz]
$H_{\alpha\alpha}$	Dynamic flexibility, $\alpha=x,y$
$K_{sx,}\ K_{sy}$	Structural (support) stiffnesses [N/m]
$L,\ D$	Length and diameter of SFD land [m]
M	Mass of bearing housing [kg]
M_f	Estimated mass of lubricant (feed plenum & recirculation annulus) [kg]
M_T	$M+M_f+D$. Dynamic mass of lubricated test system [kg]
$P_s\ ,\ P_r$	Inlet pressure and pressure at recirculation annulus [Pa]
Q	Volumetric flow [LPM]
T	Lubricant temperature [°C]
U_α	Experimental Uncertainty (α= measured variable)
V	Velocity vector [m/s]
x,y	Bearing dynamic motions along X,Y directions [m]
$\bar{x}, \bar{y}$	Frequency components of bearing motions [m]
$z_{(\omega)}$	Complex displacement in frequency domain [m]
ΔP	P_s-P_r, Pressure differential across SFD [Pa]
$\rho,\ \mu$	Lubricant density [kg/m^3] and viscosity [Pa.s]
$\omega,\ \omega_n$	Excitation frequency [rad/s], natural frequency [rad/s]
ζ	$C/[2\ (K_s M)^{1/2}\ ]$. Viscous damping ratio

I Introduction

Squeeze Film Dampers (SFDs) are widely used to provide external damping in aircraft gas turbines supported on rolling element bearings as well as in hydrocarbon compressors, for example. SFDs also aid to attenuate rotor synchronous responses at passage through critical speeds where shaft vibration amplitude due to imbalance peaks. A typical SFD consists of a stationary journal (generally the outer race of a ball bearing) and a circular housing, both separated by a small gap filled with lubricant. In operation, the dynamic motion of the journal (whirling) squeezes the thin lubricant film, thus generating hydrodynamic pressures and film forces able to dissipate mechanical energy [1].

A SFD forced performance (damping capability) depends on its geometrical configuration as well as on the operational parameters such as flow regime, type of journal motion, lubricant cavitation and air entrapment among others [2]. In particular, the latter can lead to a severe reduction of the damping force coefficients [3,4]. Air entrapment occurs at sufficiently high whirl frequencies and large vibration amplitudes where air is ingested into the lubricant film, becoming entrapped, thus severely reducing the damper forced performance [5]. The severity of air ingestion and entrapment increases with frequency and journal amplitudes. This phenomenon is more pervasive in open ends SFD configurations, where at least one of the damper ends is exposed to ambient.

Presently, with increasing rotor flexibilities and shaft speeds, high performance turbomachinery undergoes high dynamic loads and large displacements. Under these conditions, air ingestion and entrapment compromise the performance of SFDs with opened end or partially sealed configurations. Sealed SFDs prove to be less prone to air ingestion/entrapment at high frequencies, thus enhancing their performance at such frequencies. Different types of seals have been adopted (O-rings, end plates, etc.), yet there are many more seal and geometric configurations (i.e. oil feeding arrangement, grooves) used in practice and not yet thoroughly researched. This work includes the experimental study of a particular sealed SFD configuration. The configuration comprises of a mechanical contact end seal and a recirculation annulus at one end of the test damper.

II Literature Review

Squeeze Film Dampers have been a subject of study since about 45 years ago, when they were introduced as an effective mean for attenuating vibration in turbomachinery. Della Pietra and Adilleta [6,7] present a compilation of the research conducted on SFDs in the last 40 years. The authors include a complete description of SFDs, their physical characteristics, including end seal configurations, the research efforts carried out for modeling SFD forced performance, developing predictive models and validations with test data.

This review discusses previous works related to experimental parameter identification of force coefficients and those studying the influence of end seals and feeding grooves on the performance of SFDs.

San Andrés and Vance [8] present a detailed review of experimental work conducted on a SFD. The test rig comprises a journal mounted on an eccentric lobe of a stiff shaft running on ball bearings with solid steel supports. Measurements of dynamic pressure distribution in the oil film are conducted for increasing frequencies. The results show large levels of dynamic pressures at the damper central groove, thus indicating the importance of groove pressures on the overall damper force performance.

Roberts *et al*. [9] present an experimental and theoretical work focused on the parameter identification of damping and inertia force coefficients from transient response data (impact tests). The theoretical analysis includes predictions using the long and short length bearing models. A parameter identification of the decay response data yields the empirical coefficients which are compared to analytical ones. The test direct damping coefficients for a squeeze film damper with open ends show good agreement with predictions based on the short length bearing model. On the other hand, inertia and cross-coupled damping coefficients are well under predicted. Additionally, the results show that "memory effects" (frequency dependency) of the SFD damping and inertia coefficients are not significant.

Ellis *et al*. [10] present a parameter identification procedure for a squeeze-film bearing system based on the State Variable Filter (SVC) method. The method relies on the assumption that a linearized two-dimensional model is appropriate for determining the set of dynamic force coefficients in a squeeze-film bearing. The evaluation of the method comprises parameter identification from simulated data and experimental data.

Simulated input data includes increasing noise levels to asses the sensitivity of the method to signal noise as it would be presented in an actual experimentation. Noise proves to affect the accuracy of the method, particularly in a heavily damped system. Results show that the linear model may not be appropriate for high magnitudes of static eccentricity (ratio >0.5).

Levesley and Holmes [11] compare the damping capacity and general performance of various SFD configurations, including different type of end seals. Their results show that an end-sealed SFD provides more damping capacity and is less prone to the occurrence of oil vapor cavitation. The authors conclude that piston-ring end sealed SFDs have a better performance over two other end seal arrangements tested (end-chambered and end plate seals).

Diaz and San Andrés [3] use the instrumentation variable filter (IVF) method for parameter identification of n-DOF mechanical linear system, and a particularized form of the method for the parameter identification of a squeeze film damper operating with a bubbly mixture. The method, based on frequency domain analysis, proves to be a reliable tool for the identification of bearing force coefficients. The predictions of the system dynamic flexibilities fairly agree with the experimental results within the frequency range from 10 Hz to 50 Hz (natural frequency 30 Hz), and for various test conditions including different air entrapment volume percentages in the lubricant mixture. The conclusions confirm that the amount of damping provided by the test SFD is greatly affected by the amount of air ingestion.

De Santiago and San Andrés [12] identify the damping coefficients of a sealed integral SFD from rotor imbalance response tests and impact tests. Both ends of the SFD are sealed by end plates of known clearance. FE predictions of the damping coefficients present good agreement with the identified coefficients. The experiments results show that the amplitudes of rotor synchronous response at the first and second critical speeds are proportional to the imbalance displacement. Furthermore, the identified damping coefficients of the integral sealed damper are twice as large as values obtained in [1] for the same damper with no end seals.

Diaz and San Andrés [13] present two methods for identification of damping coefficients in a squeeze film damper. The first method consists on a least-squares curve fitting of the damping forces in the time domain, and the second one is based on

approximating the rotor orbit using its synchronous components (Filtered Orbit Method). The frequency domain method proves to be more adequate and simple than the time domain method. The results from the experiments show that the identified damping coefficients are insensitive to whirl frequency and nearly independent of the imbalance magnitude.

San Andrés and De Santiago [14] present experiments to obtain the dynamic parameters of an open-end squeeze film damper and comparisons of the results with the full-film short length bearing theory. The publication addresses the effects of fluid inertia as well as the effects of air entrapment on the dynamic response of the SFD. The authors show an interesting approach to predict the performance of the SFD operating with severe air entrapment. The air entrapment is accounted for as a reduction of the effective length of the damper rather than a reduction in the effective viscosity of the fluid/air film mixture (as represented in previous analytical efforts). The effective length of the SFD is frequency and amplitude dependant, as the amount of air entrapped is a function of these two variables. In the experiments presented, the effective length ranged from 82% to 78% of the actual damper length. The identified damping force coefficients agree well with predictions, except for the identified inertia coefficients that are approximately twice as large as those obtained from predictions.

III Test Rig Description

The test rig comprises of the same structure reported in a previous TRC research project [15]. Figure 1 shows a schematic view of the test rig structure. A vertical rigid shaft mounted on three precision ball bearings (natural frequency 400 Hz [14]), holds a steel journal of 5”(127 mm) diameter and 3”(76.2 mm) long. The bearing assembly consists of an acrylic bearing sandwiched by two steel plates, attached by two vertical steel plates. These plates also serve as an interface to apply external forces onto the bearing assembly. The top plate includes a connection for lubricant supply through a flexible hose, a static pressure gauge displaying the feed pressure into the bearing and four eddy current sensors facing the shaft. The composite bearing housing hangs from a top structure with four steel rods giving a structural stiffness to the test bearing section.

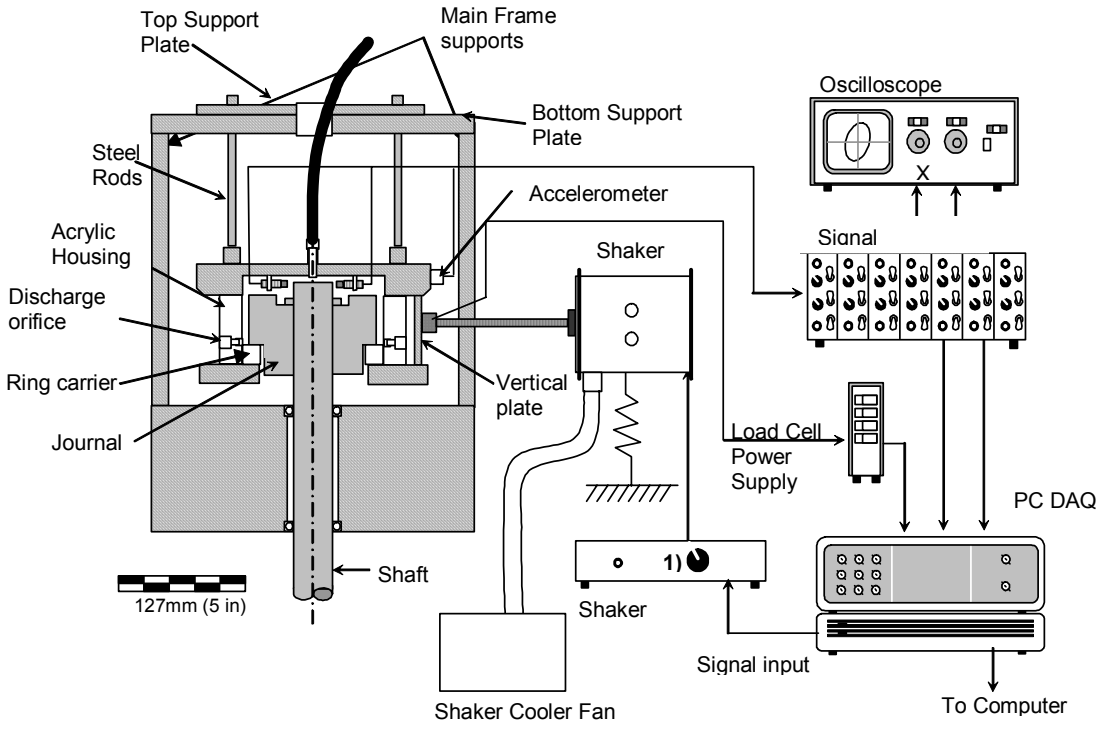

Figure 1 Test rig for dynamic force measurements and flow visualization in a sealed end SFD

A mechanism comprising two sliding flat plates (top and bottom support plates) on the top structure allows centering and off-centering positioning of the bearing with respect to the shaft [15].

Figure 2 shows the sensor disposition and reference coordinate system on the SFD housing. Two electromagnetic shakers (max. 100 lbf or 448 N), suspended from separate steel frames, stand to provide excitation forces onto the test device. Slender steel stingers connect the shaker to the bearing housing (*x* and *y* directions). Piezoelectric load cells are fastened to the side plates and the one of the stingers end. The top disk allocates two accelerometers *(x,y)*, right above the side plates.

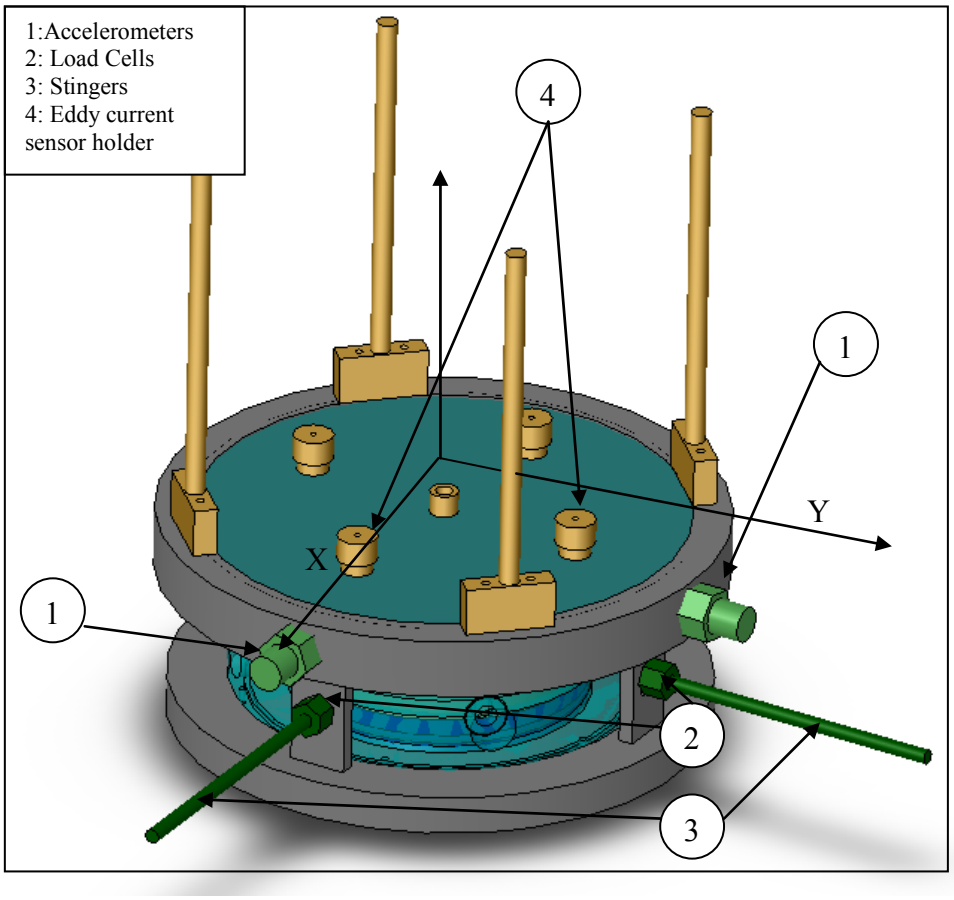

Figure 2 SFD housing reference coordinate system and location of sensors.

The bearing housing design integrates a SFD land and an annulus that accommodates a metallic ring (ring holder). This metallic ring along with the journal bottom surface provides a metal-metal mechanical seal. A wave spring, pushing the ring holder against the journal, applies a contact force between the matting surfaces. Furthermore, different sets of shims make it possible to adjust the contact force between the surfaces. Figure 3 and Figure 4 depict a cross section and a cut view of the end sealed SFD design along with its components, respectively.

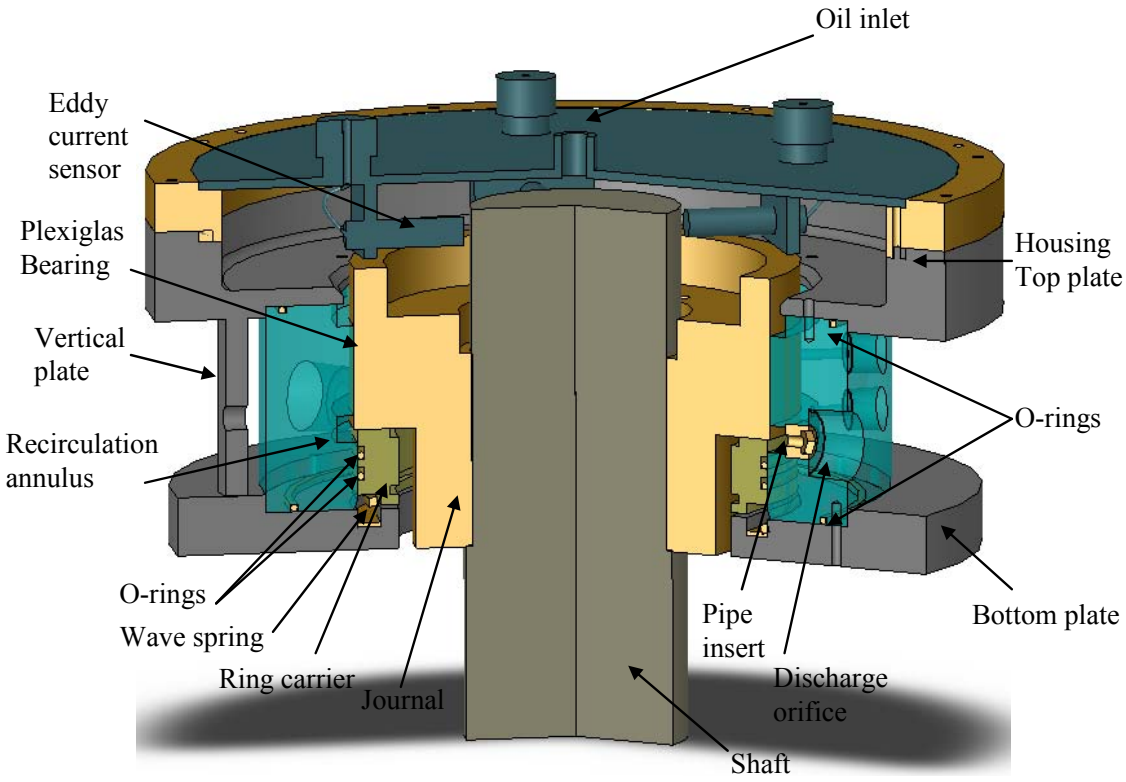

Figure 3 Sealed-end SFD assembly cross section view.

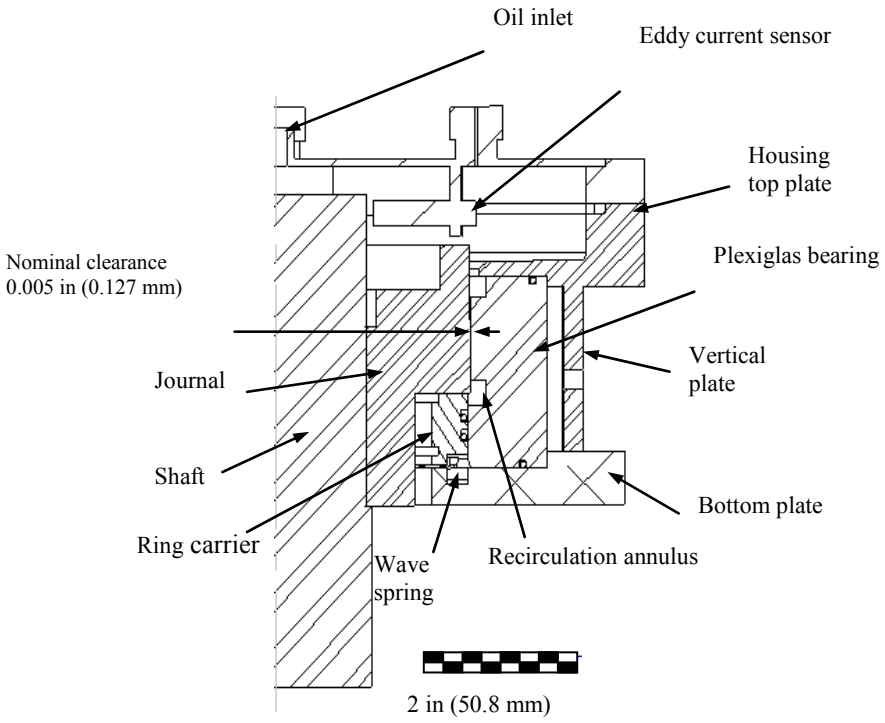

Figure 4 Sealed-end SFD assembly cut view.

III.1 Data acquisition and post-processing

A DAQ board serves as interface to connect the instrumentation, including pressure sensors, accelerometers, load cells and proximity probes to a PC. The data is recorded using a modified version of an existing Labview® virtual instrument (VI) initially designed by Diaz [16]. The modified version includes the following features to the LabView DAQ VI

- Control magnitude and frequency of 2 shakers (real time- no need to stop operation)
- Control oil pump frequency controller through and digital output (using a relay box).
- Control system to automatically adjust shaker input level to match a given load or displacement magnitude (selected by the user).
- Automated operation for multi-frequency tests.

A Mathcad® worksheet processes the recorded time traces (displacements, acceleration, forces), transform the data into the frequency domain, and perform the spectral analysis to obtain the test SFD force coefficients.

III.2 Lubrication system

Figure 5 depicts the lubrication system of the test rig, presently including two flowmeters and pipe lines for the four outlets of the new SFD configuration (end sealed). The flowmeters, located at the SFD inlet and outlet lubrication lines, allow estimation of leakage flow through the SFD end seal.

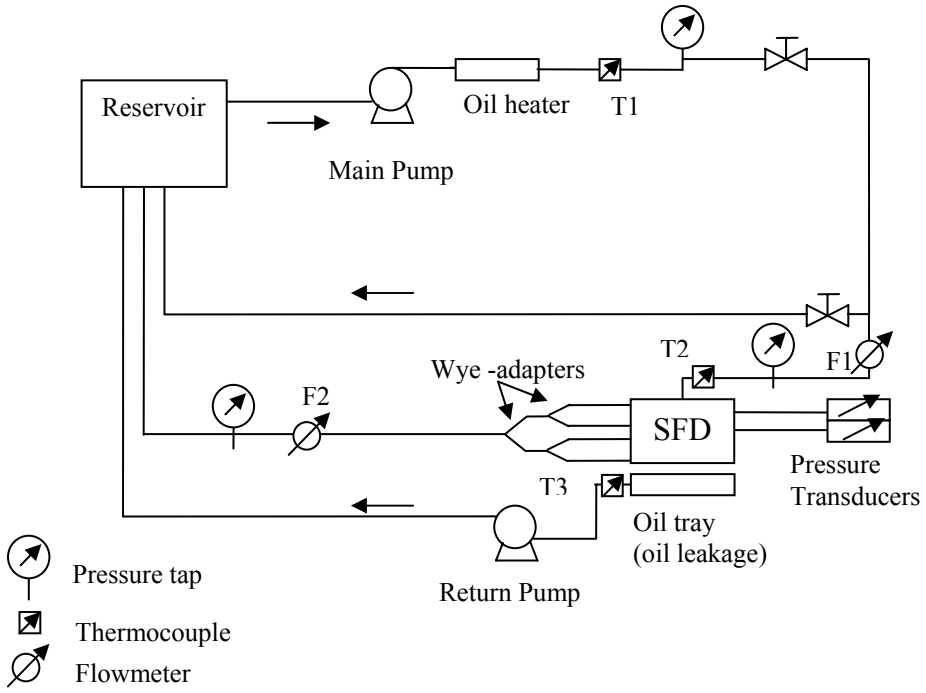

Figure 5 Schematic view of lubricant system.

The piping for connecting the SFD multiple oil outlets is symmetric in order to equalize the friction losses for each of the four outlets. This implies same longitude hoses and symmetric wye adapters.

The lubricant to be used is an ISO VG 2 with a density (ρ) of 736 kg/m^3 and its absolute viscosity follows is related to temperature (°C) by

$$\mu_{oil}(T) = 2.8e^{-0.01665(T-23.6)} \text{ cPoise} \quad (1)$$

obtained from viscosity measurements using a rheological viscometer [15].

IV Identification of Structural Parameters (Dry System)

IV.1 Static tests

The SFD assembly was separated into its components: Plexiglas bearing, top and bottom plates, and top lid. Each component is weighted using a calibrated scale (±0.01 lb). The weight of the rods and blocks (connecting the rods to the SFD assembly) is measured using a smaller scale (±0.001 lb). Table 1 shows the weight of each of the mentioned components and the estimated effective mass. Notice that for a steel rod, its effective mass is 1/4 of its total mass, since each rod is fixed as a cantilever beam.

Table 1 Measured weight and estimated effective mass of the SFD assembly and connecting rods.

	Weight [lb]
SFD Assembly [±0.01] *	14.13 (6.4 Kg)
Lid and hose connector**	6.60(3 Kg)
Rods [±0.001]	1.3 (0.59 Kg)
Blocks[±0.001]	0.25 (0.11 Kg)
Total effective mass	21.3 (9.7) (±1%)

*: including hose connectors, ring carrier and sensors.
**: including pressure sensor.

Static load tests using a force gauge (±0.5 lb) and two eddy current sensors (*X2,Y2*) yield two stiffness parameters (K_{sx}, K_{sy}). These tests were conducted without the journal in position (i.e. no rubbing interface). Figure 6 shows the bearing deflections in the *X* and *Y* directions due to a force exerted in the same direction. Each data point represents an average of a set of two static load tests. The results follow a linear tendency along the entire range of loads exerted on the SFD assembly (-89 N to 89 N). Thus, a constant stiffness coefficient in each direction (*X* and *Y*) is appropriate to characterize the rigidity of the four rods arrangement.

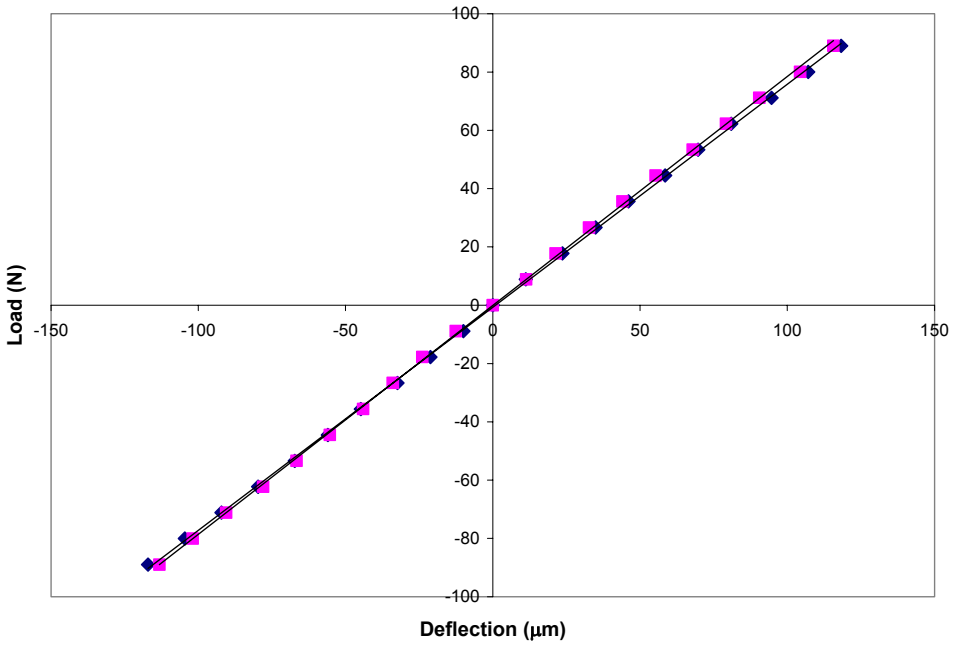

Figure 6 Bearing deflection vs. applied load in the *X,Y* direction due to a force applied in the respective (same) direction. (U_F: 0.5 lb)

Table 2 presents the structure stiffnesses in the *X* and *Y* directions. The values are very close to each other (~4% different), confirming the symmetry of the test element.

Table 2 Structural stiffness coefficients of bearing support from static tests

	K_{sx}[lb/in]	K_{sy}[lb/in]
Value	4370 (765 x10^3 N/m)	4490 (786 x10^3 N/m)
Uncertainty	175 [~4%]	180 [~4%]
Range[lb]	-20 to 20	-20 to 20
f_n* [Hz]	45±1	45±1

*: obtained using the stiffnesses and weight measured from static tests

IV.2 Impact tests

A sets of impact tests performed along the *X* and *Y* directions of the SFD assembly stand to identify the structural parameters of the SFD assembly. Figure 7 depicts the time trace of a typical impact and displacement registered in the *Y* and *X* directions, respectively.

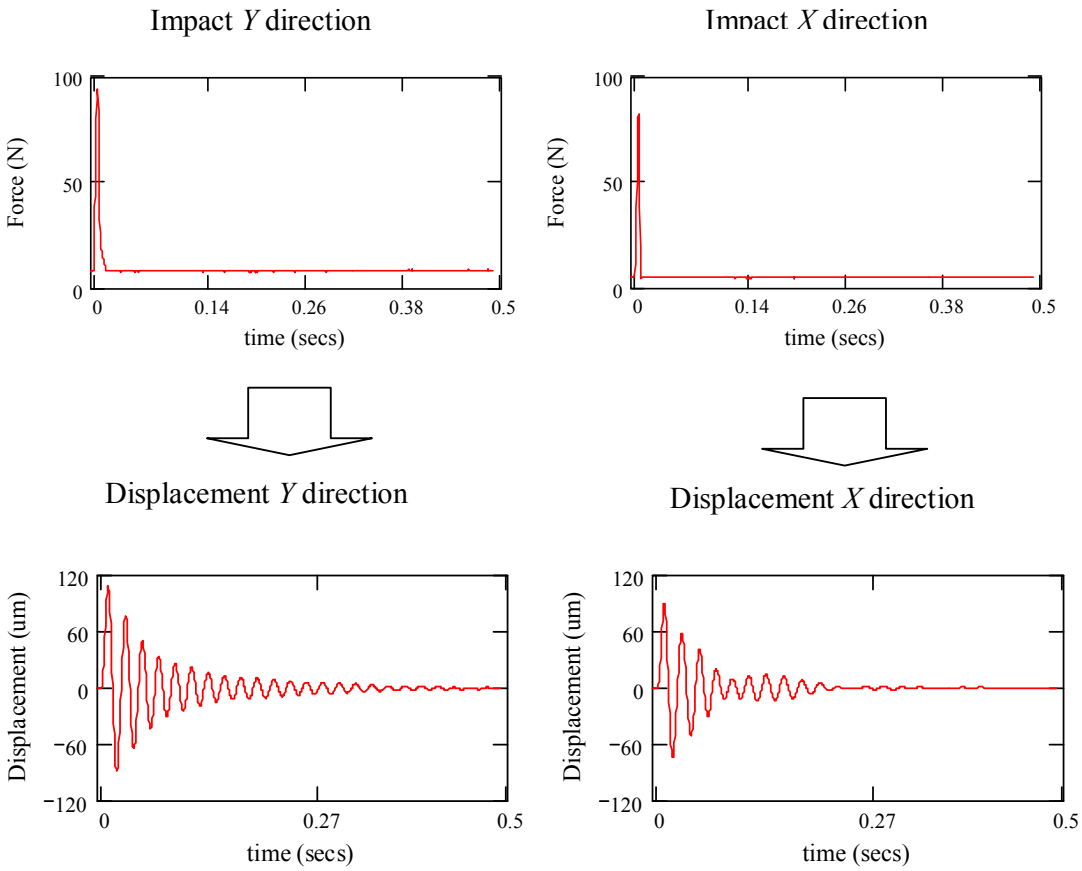

Figure 7 Impact and displacement time traces in the *Y* and *X* directions (Impact load tests)

Figure 8 and Figure 9 show the system transfer functions in the *X* and *Y* directions, respectively obtained from the impact test. Table 3 presents the results from the impact tests exerted on the bearing assembly. In Figure 8 the two resonant peaks correspond to the natural frequency of the main frame (shown in Figure 1) (~47 Hz) and the SFD assembly (~49 Hz).

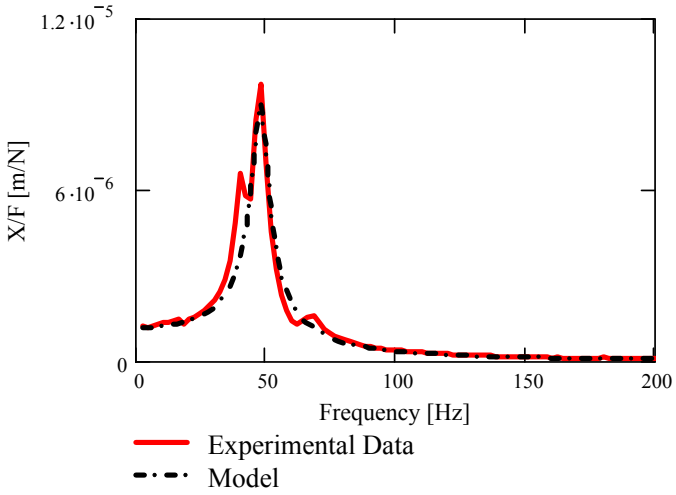

Figure 8 Transfer function and analytical fit for motions along X direction

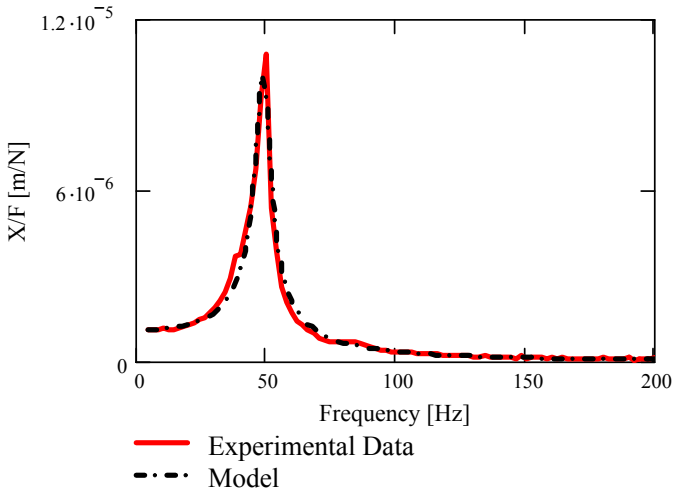

Figure 9 Transfer function and analytical fit for motions along *Y* direction

Table 3 Identified parameters from impact tests exerted on SFD test section (no lubricant)

	Parameters	*X*	*Y*
SI	Stiffness, K_s [kN/m]	800 (±40)	923 (±46)
	Mass, M [Kg]	8.8 (±0.5)	9.7 (±0.5)
	Damping, C_s [N.s/m]	367	315
US	Stiffness, K_s [lb/in]	4570 (±230)	5270 (±265)
	Mass, M [lb]	19.5 (±1)	21.5 (±1.1)
	Damping, C_s [lb.s/in]	2.1	1.8
	Damping ratio, ζ	0.069	0.052
	Natural Frequency f_n[Hz]	47 ±1	49 ±1
	R^2 (goodness of fit)	0.96	0.98

The mass estimated from the static tests (measured weight and static stiffness) is in agreement (within uncertainty) with the values obtained from impact tests in the *X* direction (~1%) and *Y* direction (~0.5%). The stiffness estimated from impact tests are similar (within ~4%) to the one obtained from static test in the *X* direction, whereas in the *Y* direction both approaches (impact load and static load tests) render different magnitudes (~15%). This discrepancy is attributed to the alignment of the impact hammer respect to the test device. The test rig has limited accessibility in the *Y* direction for correct positioning the impact hammer.

In the following, the stiffness of the test system is taken from the static load tests (uncertainty band 4%), i.e. K_{sx} = 788 kN/m, and K_{sy} =823 kN/m.

IV.3 Periodic input load tests

This section focuses on the identification of the damping characteristics of the dry system (no lubricant) with the mechanical seal in place. The aim is to asses the effect of the mechanical seal on the system damping (i.e. dry friction). Four set of single frequency excitation tests serve to characterize the damping characteristics of the system. The tests include two load magnitudes (40-39 N and 35-33 N) from 20 Hz up to 200 Hz. The excitation loads exerted along both directions have the same magnitude and are 90 0 out of phase (i.e. circular load orbit). The results in Figures 10-17 correspond to the last set of tests. Appendix C shows system responses and excitation orbits for selected frequencies.

Figures 10 trough 12 show the waterfalls of the load, displacements and acceleration magnitudes in along the X and Y directions, respectively.

Figure 10 evidences fluctuations of the load magnitude at high frequencies (from 150 Hz to 200 Hz). These fluctuations are introduced by the FFT operator (frequency resolution) and do not reflect the actual load magnitude shown in Figure 13. Figure 12 shows super synchronous components in the acceleration mainly for load excitations with frequency close to 50 Hz. Odd super synchronous frequencies evidence dry friction interaction.

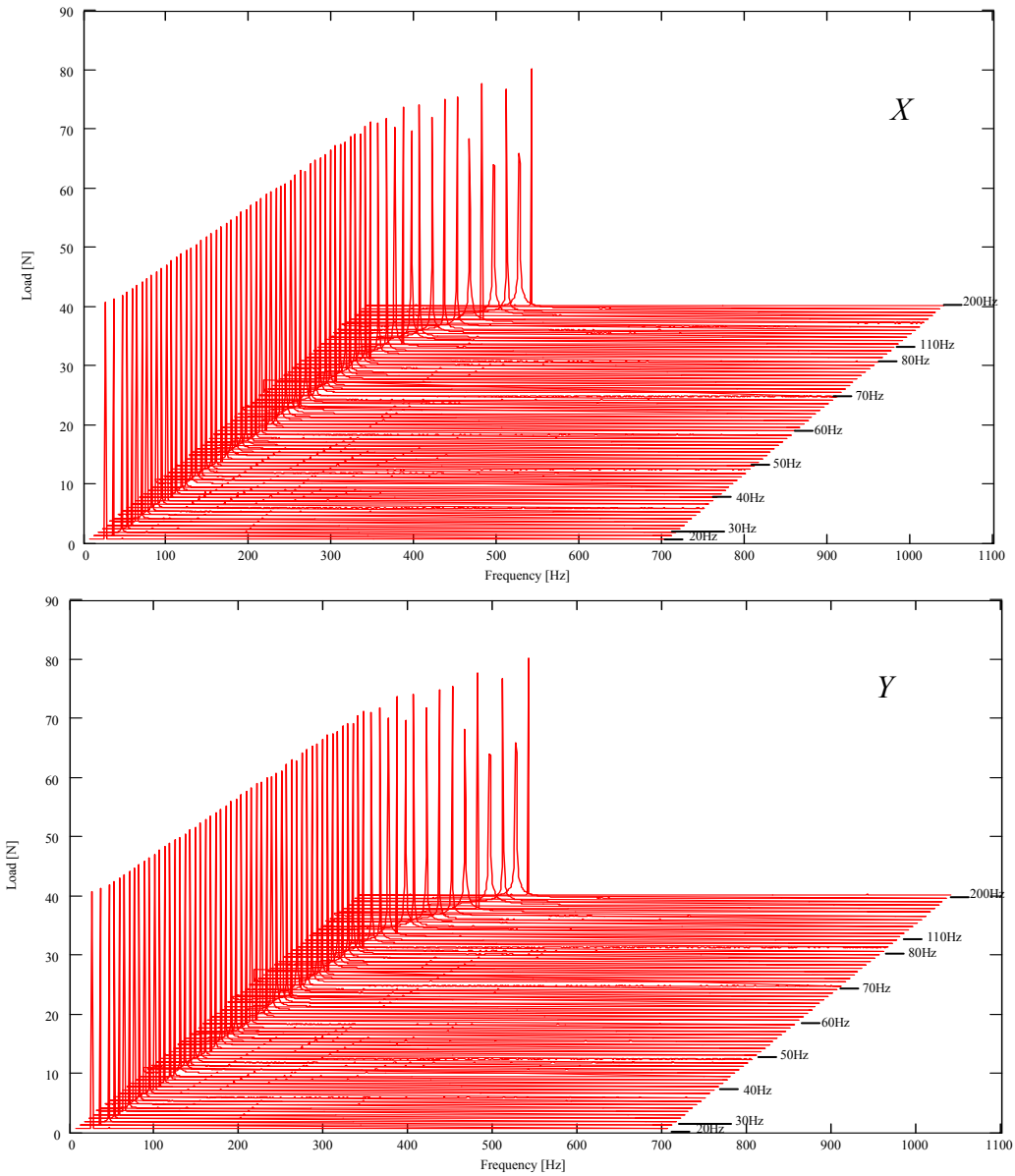

Figure 10 Waterfalls of excitation load in the *X* and *Y* directions. (Dry SFD. End seal in place. L: 40 N)

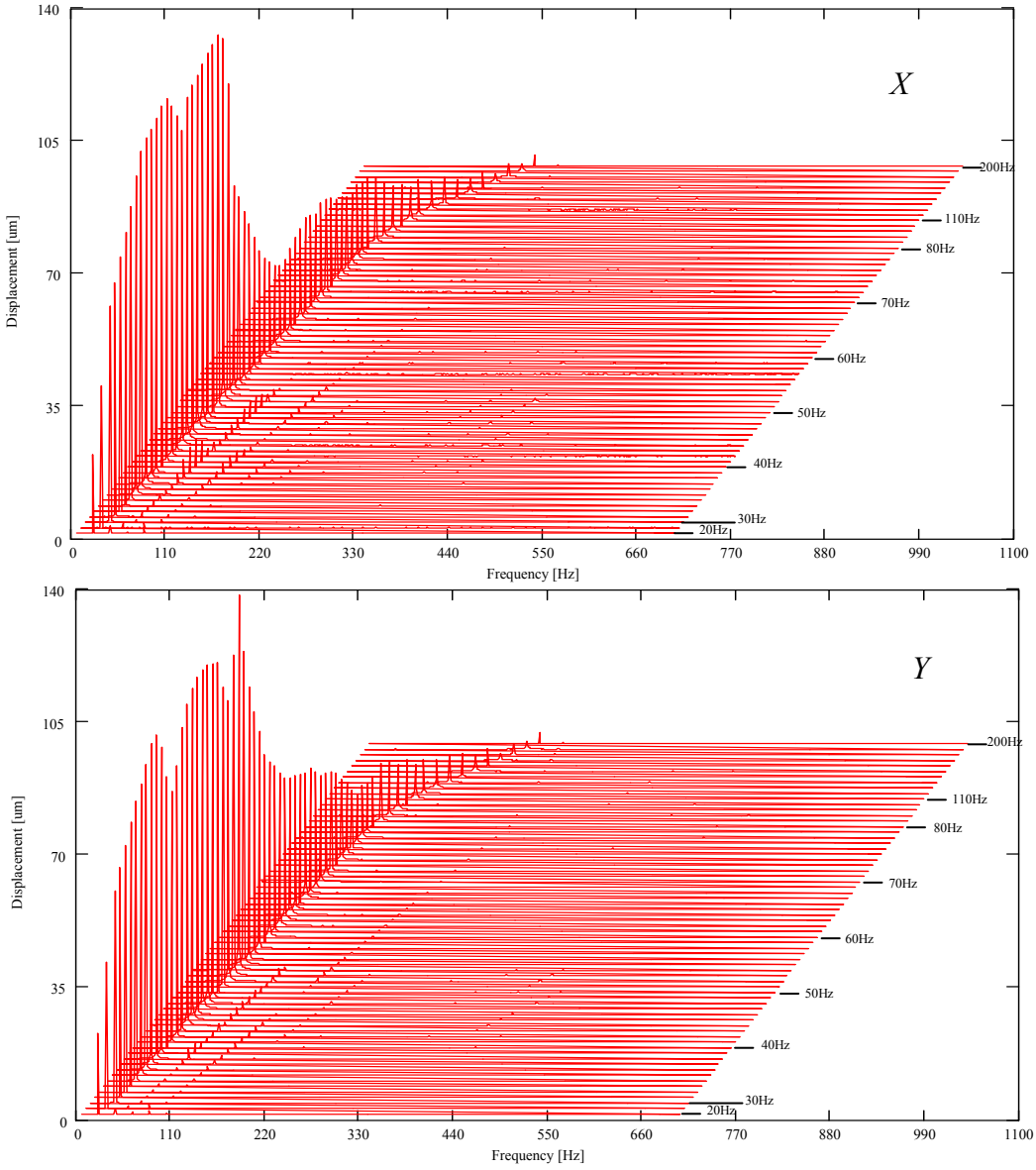

Figure 11 Waterfalls of displacement response in the *X* and *Y* directions. (Dry SFD. End seal in place. L: 40 N)

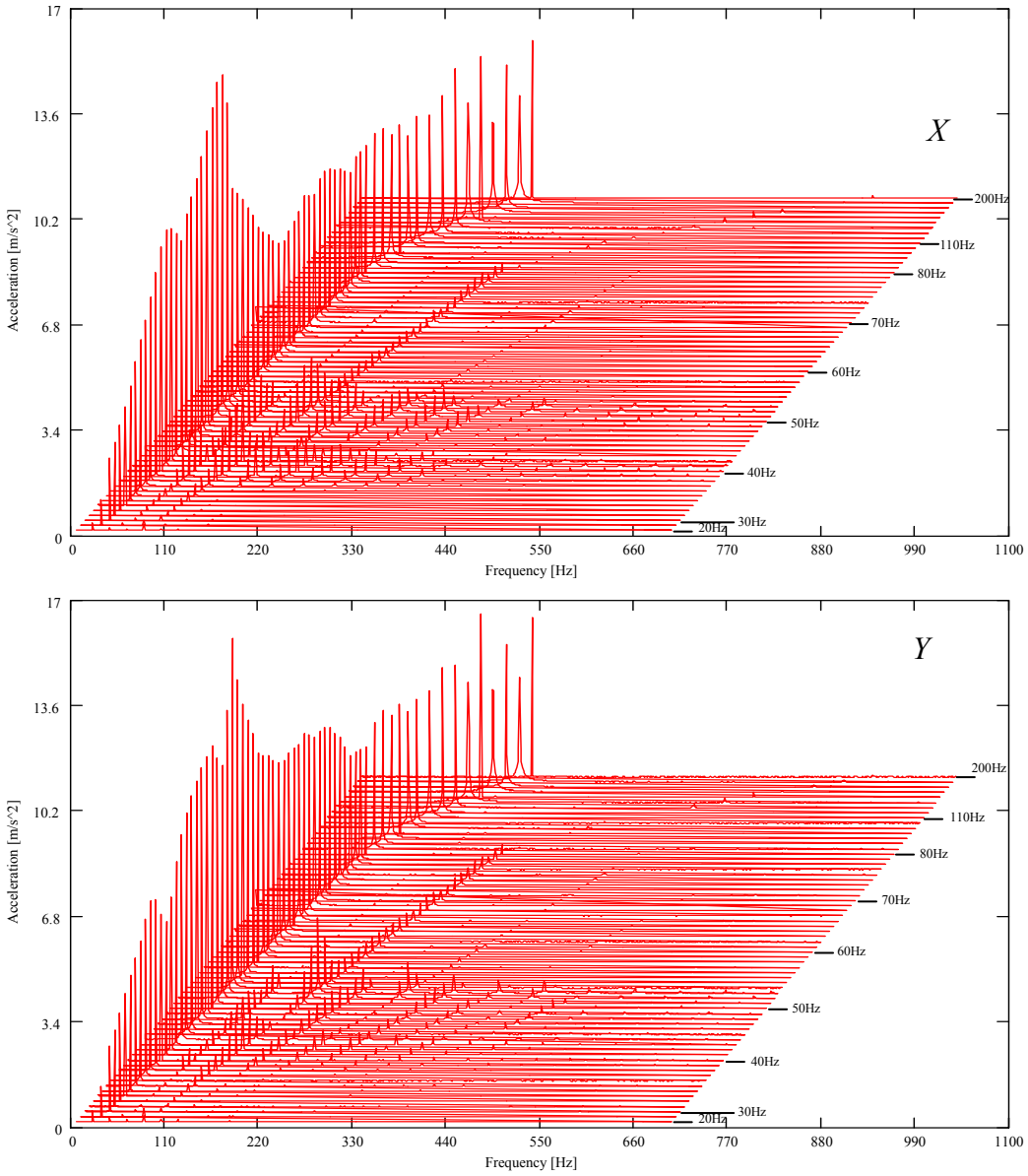

Figure 12 Waterfalls of acceleration response in the *X* and *Y* directions. (Dry SFD. End seal in place. L: 40 N)

Figure 13 shows the synchronous component of the excitation load in the *X* direction (similar in *Y*). Figure 14 and Figure 15 show the resulting synchronous displacements along the *X* and *Y* directions, respectively. There are two peaks in response (natural frequencies), one at ~39 Hz and other ~50 Hz. The first natural frequency is associated to the motion of the main frame (see Figure 1), and the second natural frequency is associated to the motion of the steel rods supporting the SFD assembly. The effect of dry friction interaction between the mating surfaces of the mechanical seal is evident in the system response. There are a number of excitation frequencies in the *X* and *Y* directions

where the system response suddenly drops, which represent transitions between slipping and sticking regimes of motion.

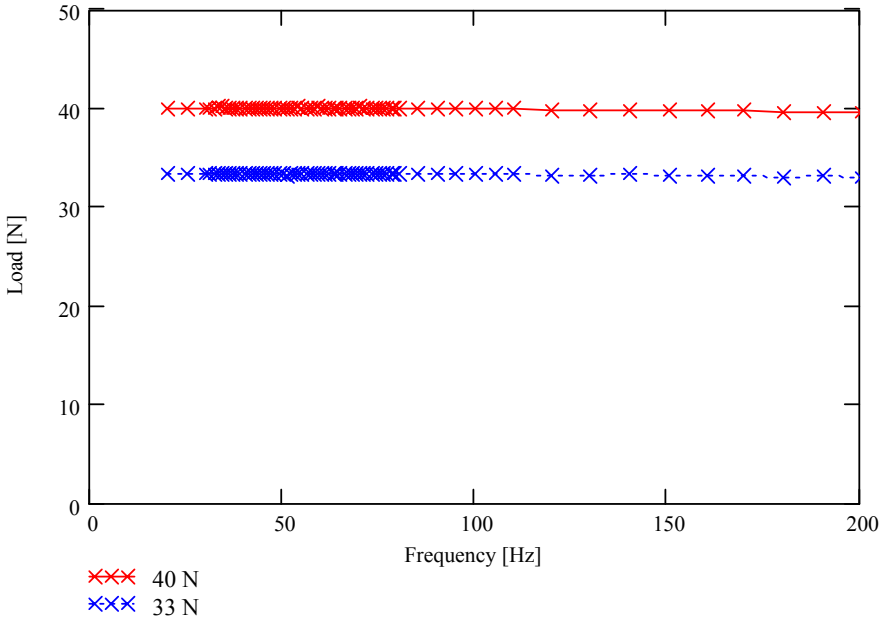

Figure 13 Input Load synchronous frequency component in the X direction. (Dry SFD, End seal in place)

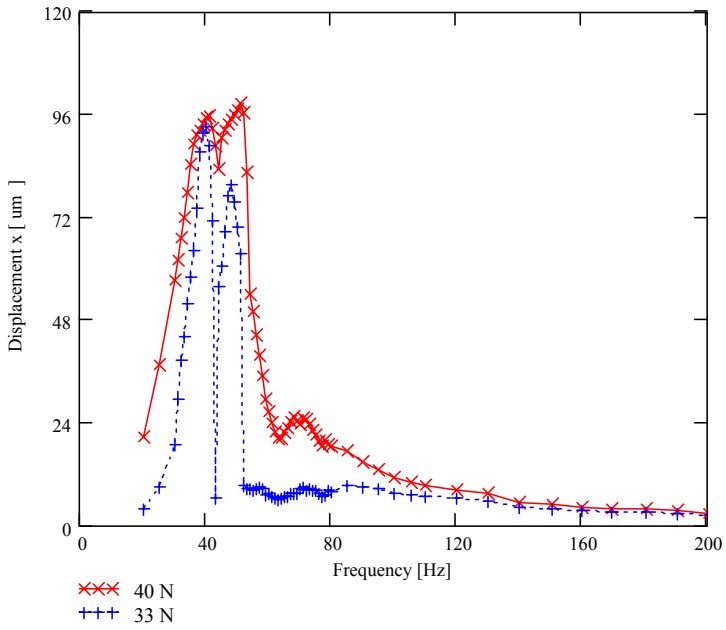

Figure 14 Synchronous frequency component of displacement response (X direction) due to a constant magnitude circular orbit excitation (40 N and 33 N). (Dry SFD, End seal in place)

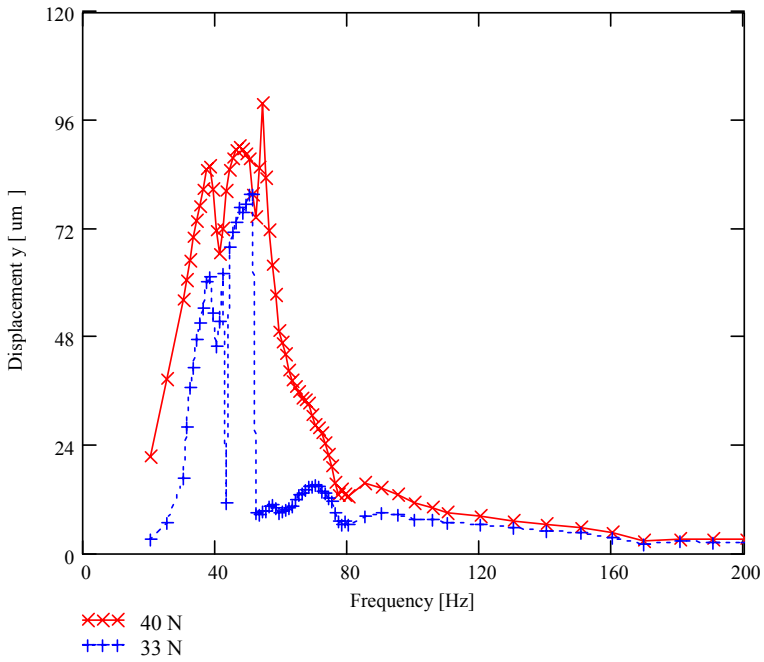

Figure 15 Synchronous frequency component of displacement response (*Y* direction)due to a constant magnitude circular orbit excitation (40 N and 33 N). (Dry SFD, End seal in place)

IV.4 Identification of dry friction force in contacting seal ring

The equivalent damping coefficient with the mechanical seal in place in place (dry system) is obtained by equating the work exerted by the external force to the energy dissipated by the system. The work exerted by the input external force is [17]

$$Work = \pi\left[\left|F_x\right|\left|X\right|\sin(\phi_1)+\left|F_y\right|\left|Y\right|\sin(\phi_2)\right] \tag{2}$$

where (F_x,F_y) and (X,Y) are the force and response vectors; ϕ_1 and ϕ_2 are the phase lag of the response relative to the force along the X and Y directions, respectively. The energy dissipated by dry friction is [17]

$$E_{dry} = F_\mu \int_{t_1}^{t_1+T} |V|\, dt \tag{3}$$

where V is the velocity vector (V_x,V_y) constructed from the displacement Fourier coefficients (no velocity data is directly available). On the other hand, some energy is also dissipated by (residual) viscous effects

$$E_{rv} = C_{rv} \int_{t_1}^{t_1+T} \left(V_x^{\,2} + V_y^{\,2} \right) dt \tag{4}$$

where $C_{rv} = C_s$ is a residual viscous damping coefficient from the support structure. The overall damping parameters are obtained assuming a combination of dry friction damping (arising from the end mechanical seal) and a residual viscous damping from other sources (i.e. steel rods, traces of oil entrapped in between ring carrier and Plexiglas bearing[1]). The identification relies on equating $E_{dry} + E_{rv} = Work$.

Table 4 shows the average of the identified friction force and equivalent viscous damping coefficient obtained from each test. The dry friction force (F_μ) and the residual viscous coefficients are obtained by finding the values that best fit the work executed by the external force (i.e. best correlation-r^2). The combination of the energy dissipated by each the dry friction and the residual viscous damping account for the total energy dissipated by the system.

The friction force relates to the magnitude of the contact force at the mechanical seal interface. Thus, the friction force can be modified by either changing the compression of the wave spring that pushes the two seal surfaces together or by replacing the spring. The current contact force (i.e. normal force) at the seal interface is estimated at 70 N (± 10 N), and represents the minimum force required to create a proper mechanical sealing of the SFD section.

The magnitude of the residual viscous damping coefficient (C_{rv}= 370 Ns/m) is similar (within ~10 %) to the one obtained from impact tests on the dry system without the seal in place (Table 3); thus representing the damping introduced by the support rods.

Table 4 Identified (averaged) dry friction force and equivalent viscous coefficients from single frequency excitation tests (20-200 Hz)

Test	Load(N)	Friction Force F_μ (N)	Residual Damping C_{rv}(N.s/m)	r^2
1	40	26	370	0.99
	35			0.99
2	40			0.98
	35			0.99
3	41			0.98
	35			0.99
4	40			0.98
	33			0.99

[1] The O-rings have to be lubricated upon assembly, which leaves oil traces in between the ring carrier and the Plexiglas bearing.

Figures 16 and 17 show the work exerted by the input force and the estimated energy dissipated by the combined damping model for each test. Figure 16 shows that the analytical model represents well the energy dissipated, even though the system shows stick-slip at certain frequencies.

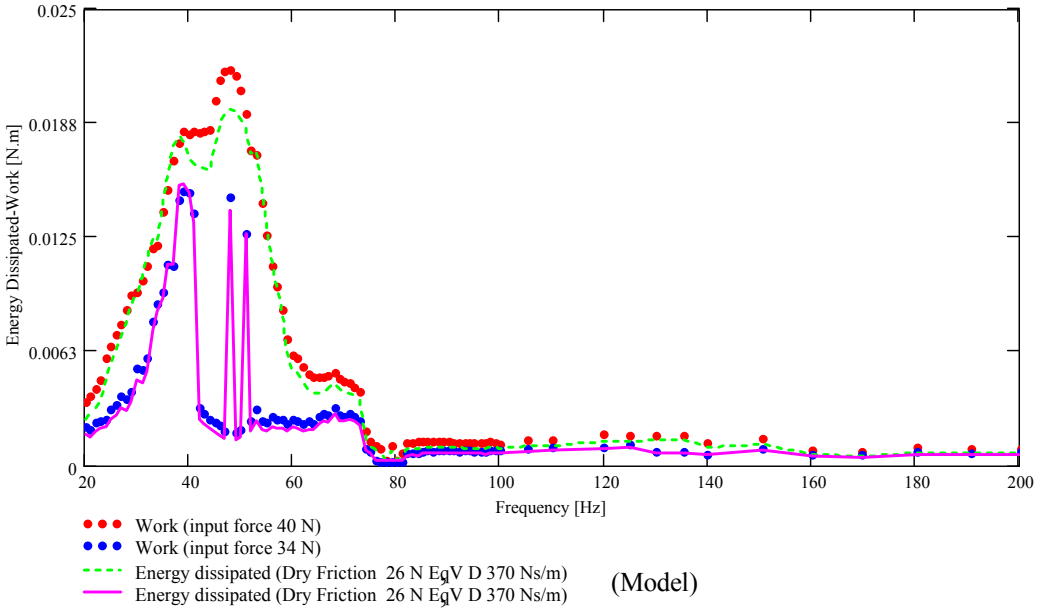

Figure 16 Work exerted by input force (= dissipated energy) estimated from combined damping model (Test 1). (Dry SFD, End seal in place)

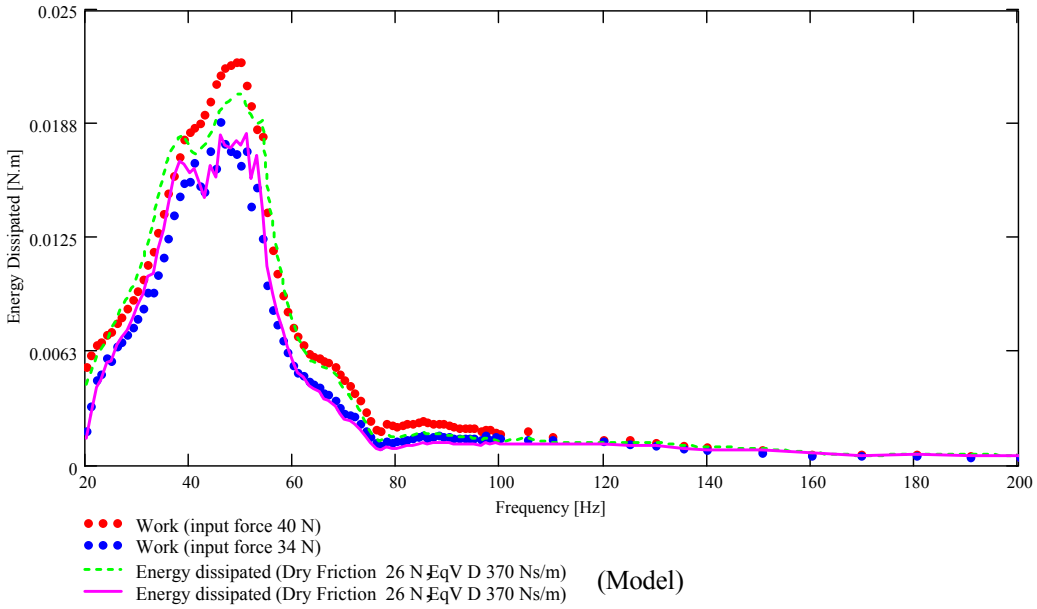

Figure 17 Work exerted by input force (= dissipated energy) estimated from combined damping model (Test 2). (Dry SFD, End seal in place)

Figure 18 presents the imaginary component of system transfer function (*F/X*) versus the excitation frequency, including the identified residual contribution ($C_{rv}\omega$, C_{rv}= 370 N.s/m). The Im(*F/X*) relates to the action of the dissipative forces on the system. For a purely viscous damping system, Im(*F/X*) = *C x ω*, a straight line with the damping coefficient (*C*) as its slope. In the figures *Im(F/X)* includes the effect of both dry friction and residual viscous damping. Notice that the viscous damping contribution, C_{rv}= 370 N.s/m, is rather small compared to the total damping of the system. This indicates that the damping arising from the seal dry friction interaction (F_{μ}= 26 N) accounts for most of the system energy dissipation. Figure 19 shows the ratio Im(*F/X*). This magnitude represents an equivalent viscous damping coefficient for the dry system. Again, the residual damping coefficient (constant with frequency) represents a minute fraction of the overall system damping. Note that the damping arising from dry friction at the contact surface is lowest at frequencies from 40 to 50 Hz, which are precisely those at which the system peaked in motion; i.e. natural frequencies.

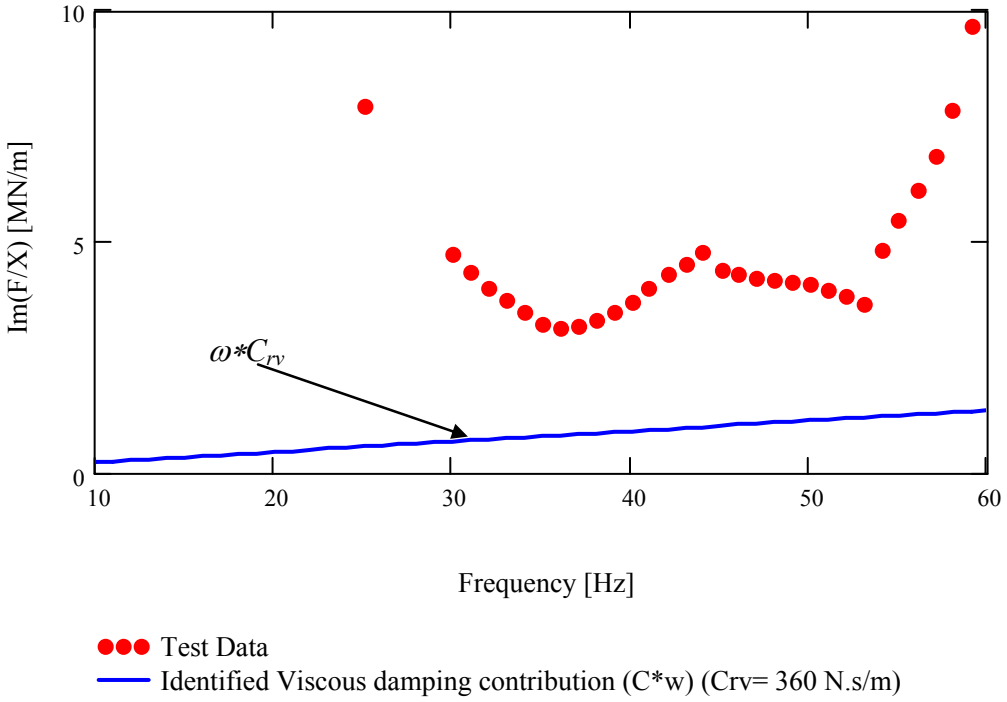

Figure 18 Imaginary component of transfer function, Im (*X/F*), vs excitation frequency. (Test 1- Dry SFD, End seal in place)

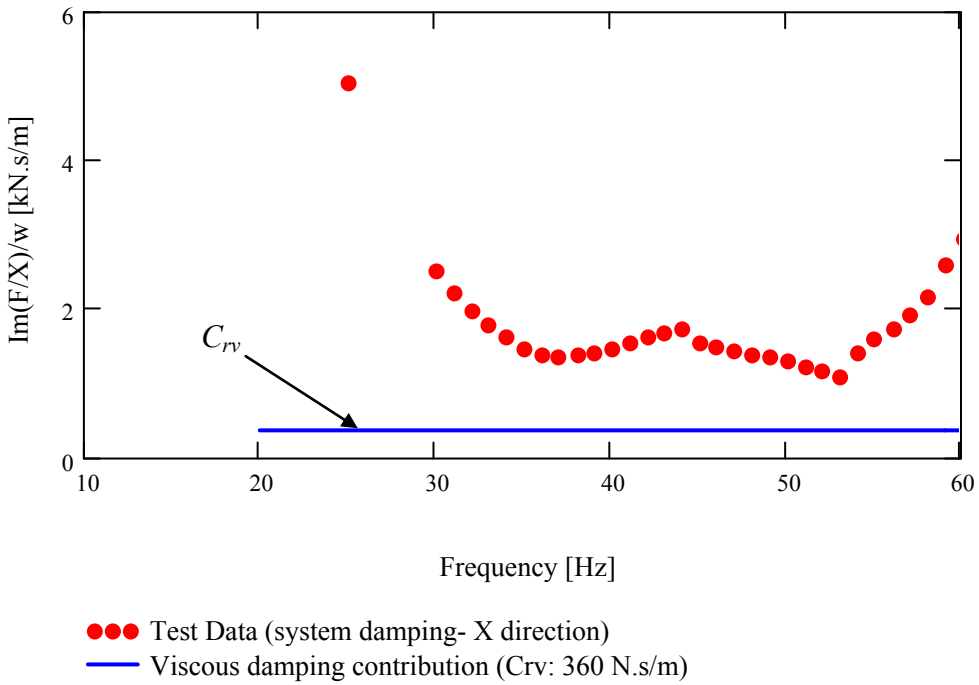

Figure 19 Equivalent viscous damping (dry friction + residual) vs excitation frequency. (Test1- Dry SFD, End seal in place)

V Measurements of flow rate in lubricated SFD

After identifying the Coulomb friction parameter of the "dry" system, lubricant ISO VG 2 is pumped trough the SFD to asses the leakage performance of the end seal. The performance of the seal is determined by verifying that the mechanical seal assembly contact force effectively prevents leakage, and thus the recirculation annulus is completely filled with oil at all times. During the flow measurement tests the seal effectively prevented oil leakage, thus indicating that the contact force at the seal interface is sufficiently large to seal the damper.

Figure 20 depicts the combined results of flow versus pressure drop from three different set of tests, including five increasing oil inlet temperatures (21-43 ^{o}C). The measurements show that, as the oil temperature increases the flow increases relative to the pressure differential across the damper.

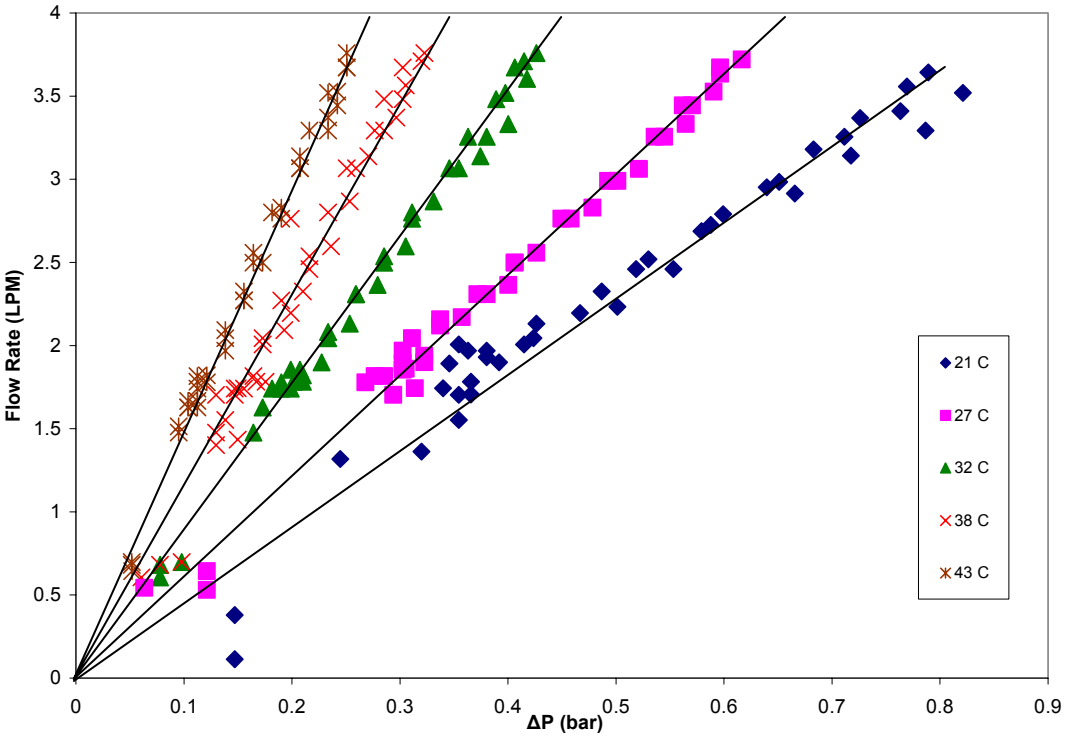

Figure 20 Lubricant Flow trough SFD vs. pressure differential

Figure 21 presents the pressure differential across the SFD versus the supply pressure. The pressure differential is clearly a linear function of the inlet pressure, and depends on the diameter of hole of the flow restrictors located at the discharge port in the recirculation annulus. Furthermore, the pressure at the recirculation annulus is close to

ambient pressure (max P_r~ 1.12 bar). The flow restrictor consists of four pipe inserts, each with a 2.8 mm (0.11in) diameter through hole, that restrict the outlet flow at the recirculation annulus. Figure 22 depicts the location of one of the flow restrictors.

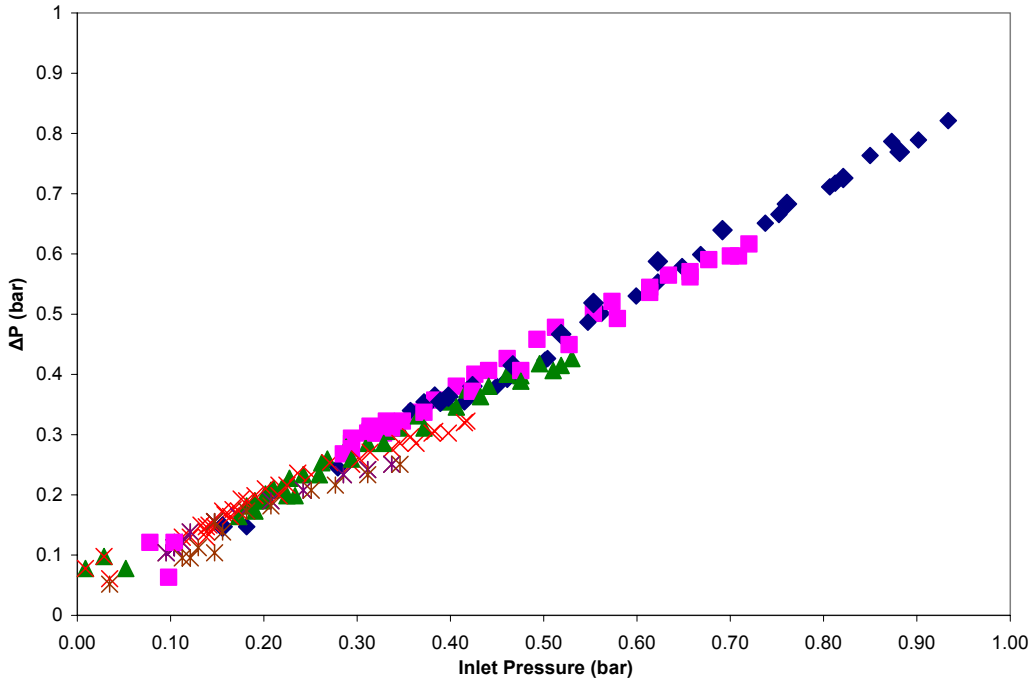

Figure 21 Pressure differential across the SFD versus inlet (supply) pressure.

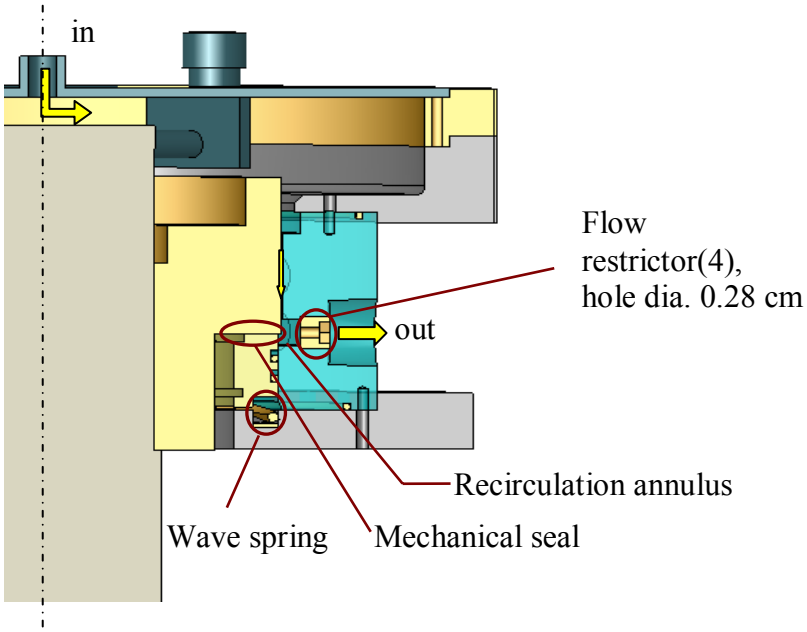

Figure 22 Cut view of SFD depicting flow restrictor.

Figure 23, shows the radial clearances, measured after each test with lubricant temperatures at 21 ^{o}C, 27 ^{o}C and 32 ^{o}C. The clearance grows significantly with increasing oil temperatures. Figure 24 depicts a representation of the growth of the SFD bearing due to the raise in temperature, as obtained from a simple finite element model using COSMOS®. The radial growth is associated to an axial growth of the SFD land and a radial growth of the steel ring inside the SFD bearing that pushes the Plexiglas bearing.

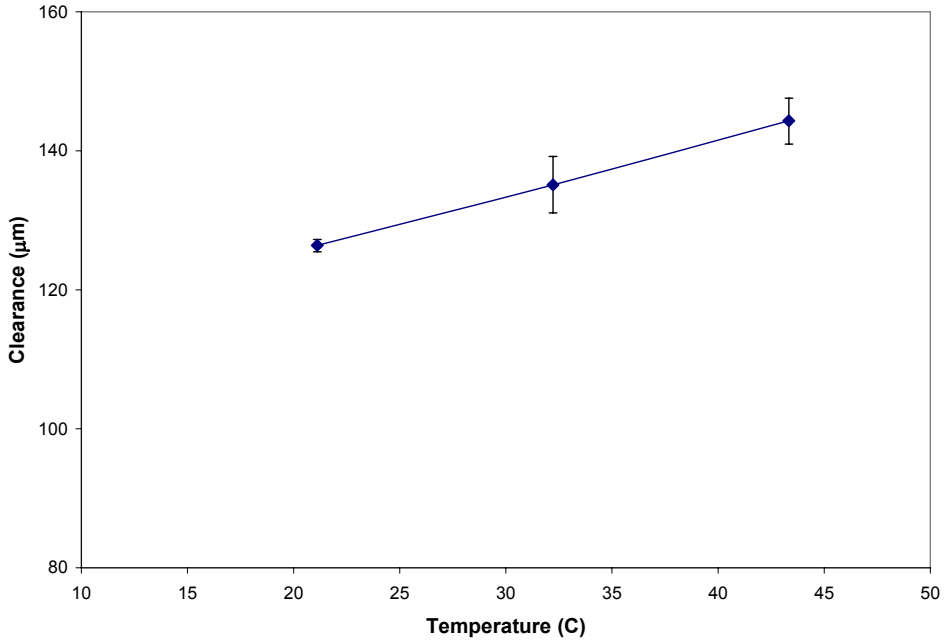

Figure 23 Measured radial clearance vs. lubricant temperature.

The analytical expression of the flow through the damper (centered journal) is [18]

$$Q = \frac{\pi D c^3}{12\mu(T)} \frac{\Delta P}{L} \tag{5}$$

where (c, D, L) are the damper radial clearance, diameter and length, respectively; ΔP is the pressure drop across the film land; and μ is the lubricant viscosity, a function of the mean film temperature (T).

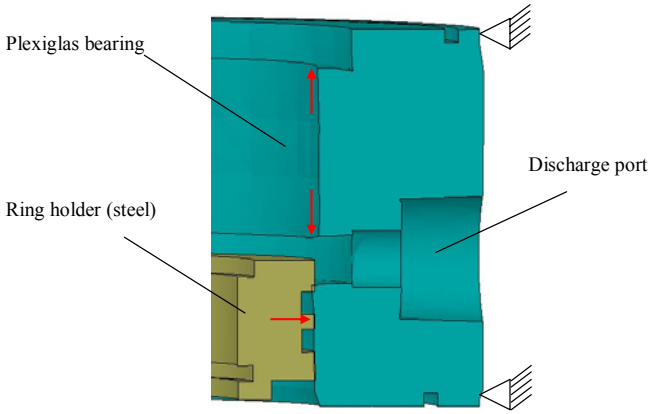

Figure 24 Representation of SFD deformation due to thermal stresses

A flow ratio is obtained by dividing the recorded flow rates by the analytical expression of flow through the damper (Eq (5)). Figure 25 shows the flow ratio as a function of the pressure differential ratio. The results are consistent, lying within a 16% band around the unit value for ΔP greater than 0.4. However, the difference of the results from a unit value indicates the need for accurate values of viscosity from Eq.(1), and the clearance growth obtained experimentally. For lower pressure differentials the flow is too small for the instruments (i.e. flowmeters) to make an accurate measurement. However, since the flow is linear with pressure differential, the flow at pressure differentials less than 0.4 can be estimated by extrapolating the flow for greater pressure differentials.

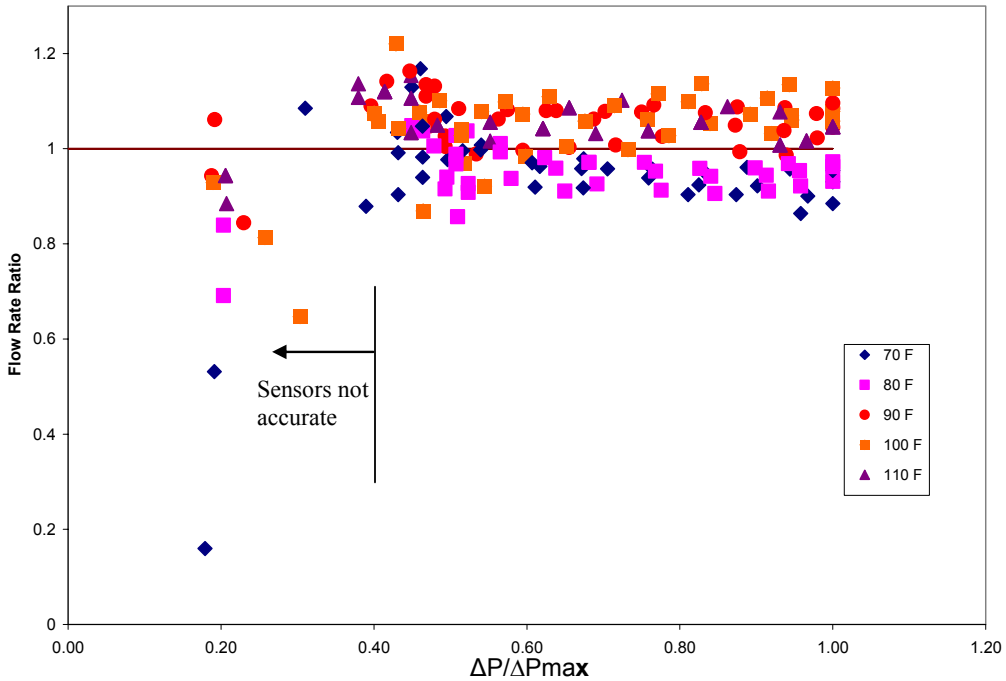

Figure 25 Ratio of test flow rate to predicted flow rate vs. pressure differential ratio

VI Identification of Damping Coefficient for Lubricated SFD from Synchronous Excitation Responses

VI.1 Experimental procedure

The first experiments consist of unidirectional periodic excitation load tests, from 20 Hz to 60 Hz, along two orthogonal directions (i.e. *X* and *Y*). The tests include five increasing motion amplitudes (13 μm to 39 μm) at each excitation frequency. The bearing is initially centered with its journal. The SFD radial clearance is 127 μm at the test temperature (23 ^{0}C). The DAQ system automatically adjusts the excitation load amplitude at each frequency to maintain the desired bearing displacements throughout the test frequency range. Maintaining a constant displacement or load magnitude provides a favorable scenario for the identification of systems that include dry friction [19]. Table 5 shows the test conditions and Appendix D includes displacements at selected frequencies from 20 Hz to 60 Hz.

Table 5 Test conditions for Dynamic load Tests. Lubricated SFD

Inlet Pressure (P_s)	15.5 kPa (2.25 psi)
Outlet Pressure (P_r)	5.7 kPa (0.75 psi)
Frequency Range	20-60 Hz (10 Hz step)
Lubricant temperature (T)	23-25 ^{0}C (73-77 ^{0}F)
Viscosity (μ)	3.17 cP
Clearance (c)	127 μm (5 mils)
Displacement amplitude (radial)	13-38 μm (0.5-0.15 mils)

Figures 26 and 27 display waterfalls of load, displacement and acceleration for 13 μm and 39 μm dynamic displacements, respectively. The acceleration shows a 3X super-synchronous component that evidences the presence of dry friction. The displacements also show a 3X component though very small when compared to the synchronous component (>1%), a clear indication that the system operates in a macro-slip regime of motion.

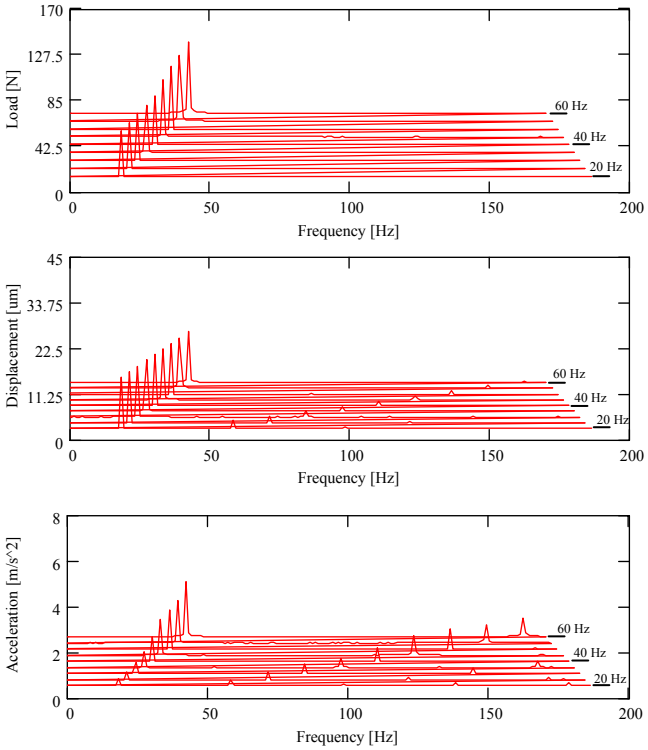

Figure 26 Waterfalls of *X*-excitation load, displacement and acceleration response from unidirectional dynamic tests (Displacement amplitude along *X* : 13 μm, Lubricated SFD)

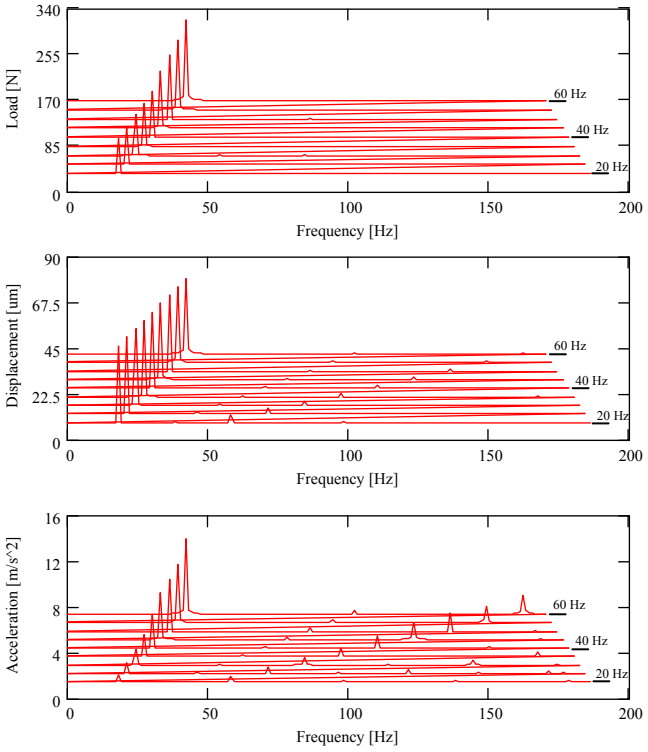

Figure 27 Waterfalls of *X*-excitation load, displacement and acceleration response from unidirectional dynamic tests (Displacement amplitude along *X* : 39 μm, Lubricated SFD)

Figure 28 depicts the synchronous component of the applied dynamic load. The load increases steadily with frequency to maintain a constant displacement. The results demonstrate that system is over damped, as the transfer function (X/F) does not show any resonance peak. Figure 29 shows the synchronous frequency component of the displacements response, evidencing a constant displacement magnitude for each test.

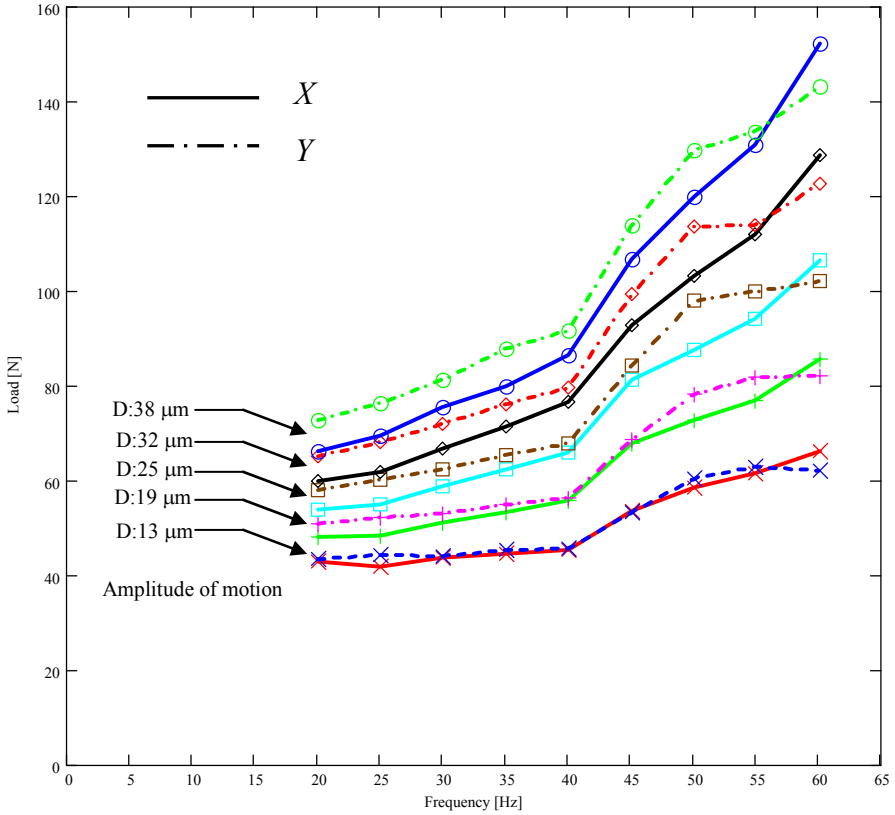

Figure 28 Amplitude of external dynamic Load vs excitation frequency (5 tests- *X* and *Y* directions, Lubricated SFD)

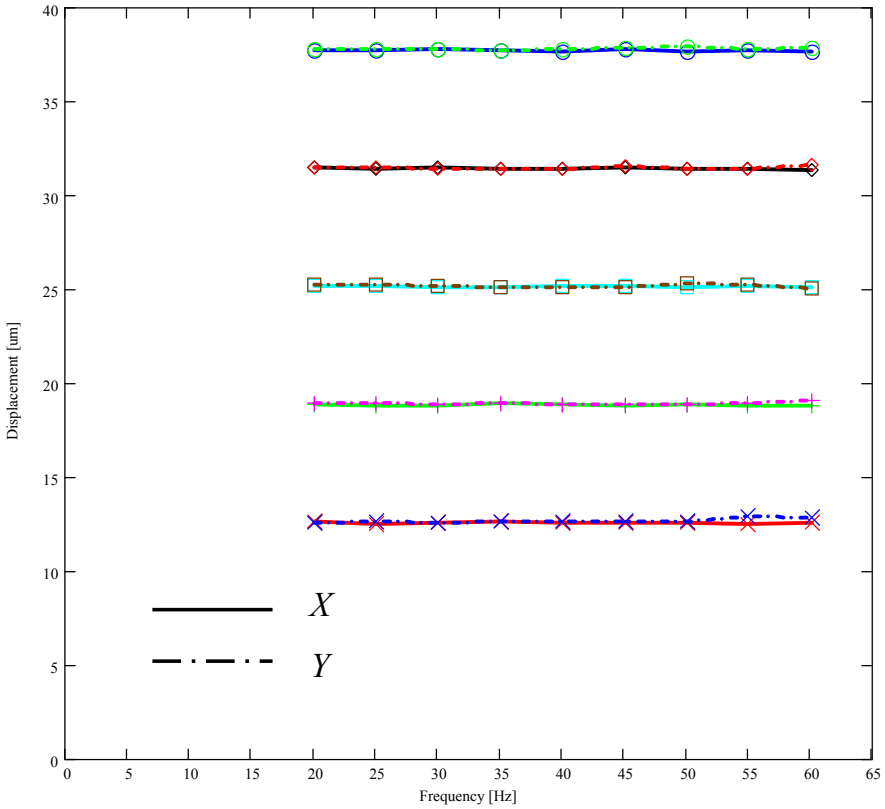

Figure 29 Fundamental amplitude of bearing motion vs excitation frequency. Periodic unidirectional load (5 tests- *X* and *Y* directions, Lubricated SFD)

VI.2 Parameter identification method

The estimation of system parameters from unidirectional load excitations follows a simple procedure in the frequency domain. The equations of motion for the test bearing section are[2]

$$\begin{bmatrix} M+M_f & 0 \\ 0 & M+M_f \end{bmatrix} \begin{Bmatrix} \ddot{x} \\ \ddot{y} \end{Bmatrix} + \begin{bmatrix} K_{sx} & 0 \\ 0 & K_{sy} \end{bmatrix} \begin{Bmatrix} x \\ y \end{Bmatrix} = \begin{Bmatrix} F_x \\ F_y \end{Bmatrix} - \begin{Bmatrix} F_x \\ F_y \end{Bmatrix}_{seal} - \begin{Bmatrix} F_x \\ F_y \end{Bmatrix}_{SFD} \tag{6}$$

M_f (0.62 ± 0.01 kg) represents the mass of fluid enclosed in the plenum above the fluid film land section and in the recirculation annulus. This mass is estimated by forced displacing the lubricant inside the test section and weighing it.

The SFD reaction forces follow the linearized description:

[2] In Eq. (6), M= 9.7 kg, K_{sx}=788 kN/m, K_{sy} = 823 kN/m as given in Tables 1-3.

$$\begin{Bmatrix} F_x \\ F_y \end{Bmatrix}_{SFD} = \begin{bmatrix} C_{xx} & C_{xy} \\ C_{yx} & C_{yy} \end{bmatrix} \begin{Bmatrix} \dot{x} \\ \dot{y} \end{Bmatrix} + \begin{bmatrix} D_{xx} & D_{xy} \\ D_{yx} & D_{yy} \end{bmatrix} \begin{Bmatrix} \ddot{x} \\ \ddot{y} \end{Bmatrix} \tag{7}$$

where $\{C_{\alpha\beta}\}_{\alpha\beta=x,y}$, $\{D_{\alpha\beta}\}_{\alpha\beta=x,y}$ are the damping and inertia force coefficients, respectively.

Recall that a squeeze film damper does <u>not</u> generate stiffness coefficients. Furthermore, as observed in preliminary testing, the cross-coupled damping and mass terms are negligible since the end seal effectively prevents air-entrapment into the damper at the test frequencies. Thus, the *X* and *Y* motions are uncoupled. For prediction purposes, the 2π-film (uncavitated) model should be appropriate. The analysis also includes the residual viscous damping coefficient, C_{rv} ~ 370 N s/m (2.11 lbf s/in).

The dry friction force from contact at the mechanical seal equals

$$F_z = F_\mu sign(\dot{z}) = C_{seal_z}\dot{z}, \quad z = x, y \tag{8}$$

where *z* is a generic displacement along *x* or *y* directions; and [17]

$$C_{seal_z} = \frac{4F_\mu}{\pi\omega|z|} \tag{9}$$

is the equivalent viscous coefficient for the mechanical seal.

In the frequency domain the system response is

$$\left[C_{tz} + \frac{i}{\omega}\left(\omega^2 M_{tz} - K_{sz}\right)\right]\dot{z}_{(\omega)} = F_{(\omega)} \tag{10}$$

where

$$M_{tz} = M_{zz} + M_f + D_{zz}, \text{ and } C_{tz} = C_{zz} + C_{seal_z} + C_{rv}, \quad z = x, y \tag{11}$$

and $z_{(\omega)}$, $F_{(\omega)}$ are the discrete Fourier Transform (DFT) of the time varying displacements and forces, respectively. In particular, a periodic forcing function can be represented as

$$F_z(t) = F_{zc}\cos(\omega t) + F_{zs}\sin(\omega t) = \left(F_{zc} - i\,F_{zs}\right)e^{i\omega t} = \bar{F}_z\, e^{i\omega t} \tag{12}$$

Subsequently, the displacement, velocity and acceleration are also periodic with identical frequency (ω), and expressed as

$$z_{(\omega)} = (z_c - i\, z_s)\, e^{i\omega t} = \mathbf{Z}\, e^{i\omega t};\ \dot{z} = i\omega \mathbf{Z}\, e^{i\omega t};\ \ddot{z} = -\omega^2 \mathbf{Z}\, e^{i\omega t} \tag{13}$$

The system damping and mass parameters can be readily identified from Equation (10) as

$$C_{tz} = \mathrm{Re}\left(\frac{F_z}{\dot{z}}\right),\quad \left(K_{sz} - \omega^2 M_{Tz}\right) = -\omega\, \mathrm{Im}\left(\frac{F_z}{\dot{z}}\right),\ z=x,y \tag{14}$$

VI.3 Results: Dynamic force coefficients for lubricated system

This section presents the SFD added mass and damping force coefficients identified from the unidirectional periodic load tests with lubricant flowing through the damper. The added inertia term (D_{xx}, D_{yy}) are extracted from the dynamic stiffness for the largest amplitude of motion tested (38 μm), provided that the mass of the housing (M) and the mass of the fluid enclosed in the damper (M_f) are available. Table 6 presents the estimated total mass coefficient and the resulting inertia coefficient, and a prediction of the added inertia coefficient for an uncavitated squeeze film. The model predictive formula is

$$D_{xx} = D_{yy} = \frac{1}{2}\frac{\rho \pi R (2L)^3}{10c} \tag{15}$$

which delivers a more realistic value than that found in the archival literature [2].

Table 6 Inertia coefficient identified from unidirectional periodic load tests (amplitude of motion: 38 μm, Frequency range 20-60 Hz)

Parameter	*xx*	*yy*
Stiffness coefficient, (K_s)[kN/m]	788	823
Total Mass, (M_t) [kg]	19.7	18.4
Fluid Mass, (M_f) [kg]	0.62	
Housing Mass, (M) [kg]	9.7	
Added mass coefficient, (D) [kg]	**9.4**	**8.1**
R^2	0.98	0.96
Predicted added mass (D) [kg]	**8.2**	

Table 6 indicates that the predicted added mass coefficient (8.2 kg) correlates well with the experimental values. Figure 30 shows the test derived dynamic stiffness for the 38 μm motion amplitude test, including the analytical model using the stiffness determined from static load and impact load tests and the total mass given in Table 6. The reported mass coefficient is determined using the largest amplitude of motion (38 μm).

Appendix F reports the added mass coefficients identified for other test amplitudes of motion.

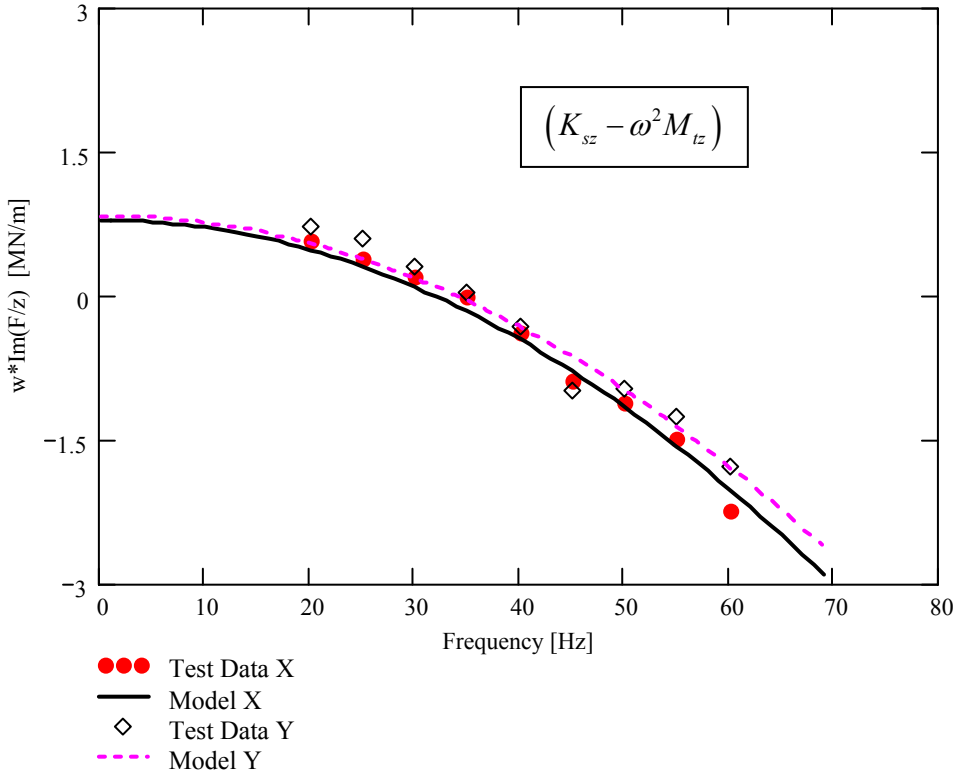

Figure 30 Dynamic stiffnesses from periodic unidirectional excitation tests and analytical model (*D*: 39 μm, K_{sx}= 788 kN/m, K_{sy}= 823 kN/m, Lubricated SFD)

Figures 31 through 34 depict the test system and SFD (alone) damping coefficients identified at each excitation frequency. The total damping combines damping from the mechanical seal (Coulomb-type damping), the viscous squeeze film, and the residual structure viscous damping. The test results show that the system is highly over damped.

The "viscous" damping arising from dry friction is inversely proportional to the amplitude of motion and excitation frequency, i.e. $C_{seal} \sim F_{\mu}/(\omega|z|)$. Therefore, "dry friction" damping is dominant at low frequencies and low amplitude of motions. On the other hand, the squeeze film damping coefficient is expected to be nearly a constant, independent of excitation frequency, function of the amplitude of dynamic displacement.

Figures 32 and 33 depict the total identified viscous damping coefficients (C_{tx}, C_{ty}) for the largest and smallest amplitudes (13 μm and 38 μm) of motion versus excitation frequency, respectively. For both dynamic displacements, the system damping coefficients decrease with frequency, but for the 13 μm displacement amplitude the

damping is considerably higher at low frequencies; thus confirming the significant contribution of the mechanical seal dry friction into the overall viscous damping.

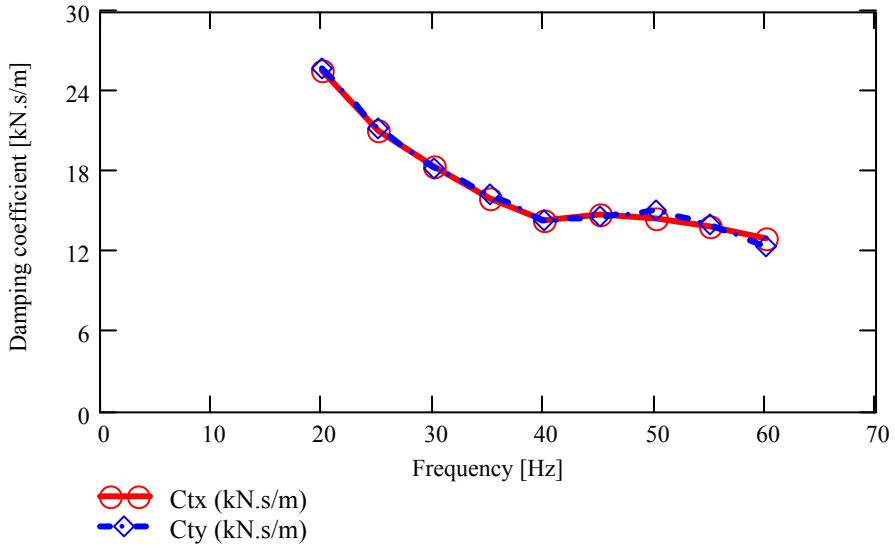

Figure 31 Identified system damping coefficients (C_{tx}, C_{ty}) versus excitation frequency. (Displacement amplitudes along *X* and *Y* : 13 μm, Lubricated SFD)

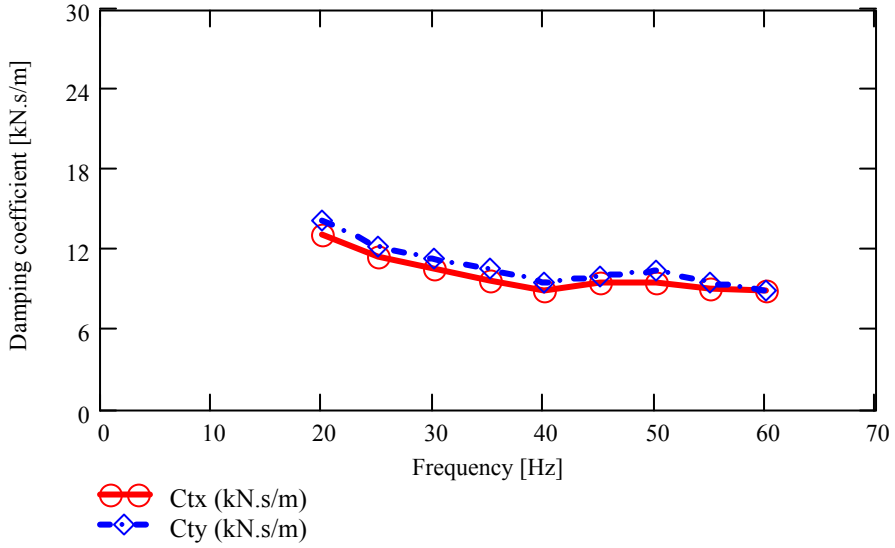

Figure 32 Identified system damping coefficients (C_{tx}, C_{ty}) versus excitation frequency. (Displacement amplitudes along *X* and *Y*: 38 μm, Lubricated SFD)

Subtracting the "dry friction" damping (C_{seal}) and residual damping (C_{rv}) from the system damping coefficients, yields the viscous damping coefficient for the squeeze film alone, i.e. $C_{xx}=C_{tx}-C_{seal}-C_{rv}$. Figures 33 and 34 depict the SFD damping coefficients extracted from the 13 μm and 38 μm dynamic displacement tests, respectively. The

coefficients ($C_{xx,}$ C_{yy}) are nearly constant and very similar for both displacement amplitudes. Appendix F presents the identified viscous coefficients for all the frequencies and amplitudes of motion tested.

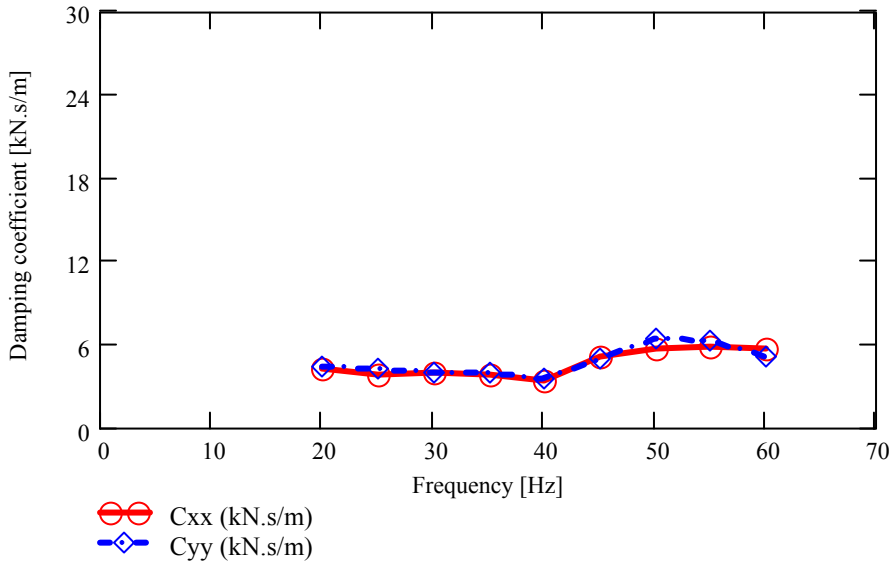

Figure 33 SFD damping coefficients (C_{xx}, C_{yy}) versus excitation frequency. (Displacement amplitudes along *X* and *Y*: 13 μm, Lubricated SFD)

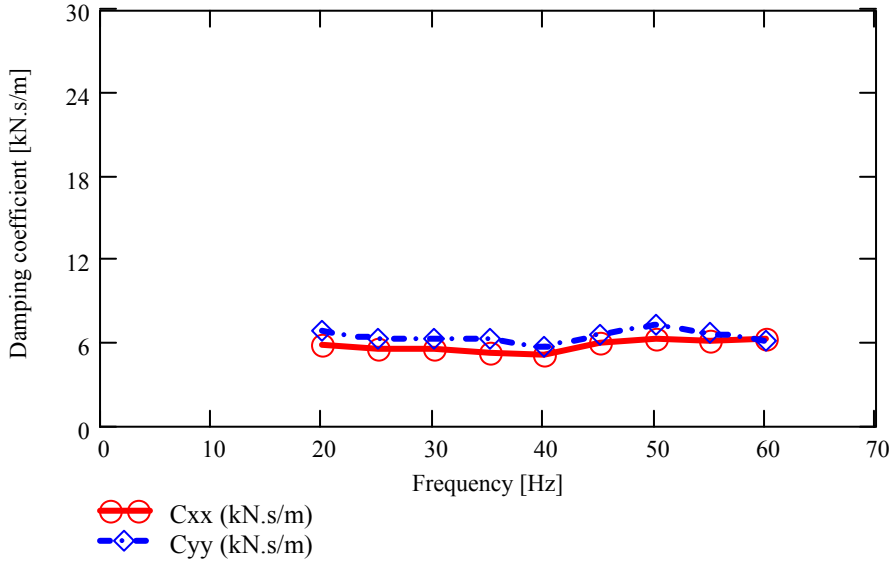

Figure 34 SFD damping coefficients (C_{xx}, C_{yy}) versus excitation frequency. (Displacement amplitudes along *X* and *Y*: 38 μm, Lubricated SFD)

Figure 35 depicts the system damping coefficients ($C_{tx,}$ C_{ty}) versus displacement amplitude for excitations at 20 Hz and 60 Hz. (C_{tx}, C_{ty}) magnitudes are largest for the

smallest amplitudes of dynamic motion, in particular at the lowest test frequency, thus evidencing the effect of dry friction interaction upon the dissipation features of the system.

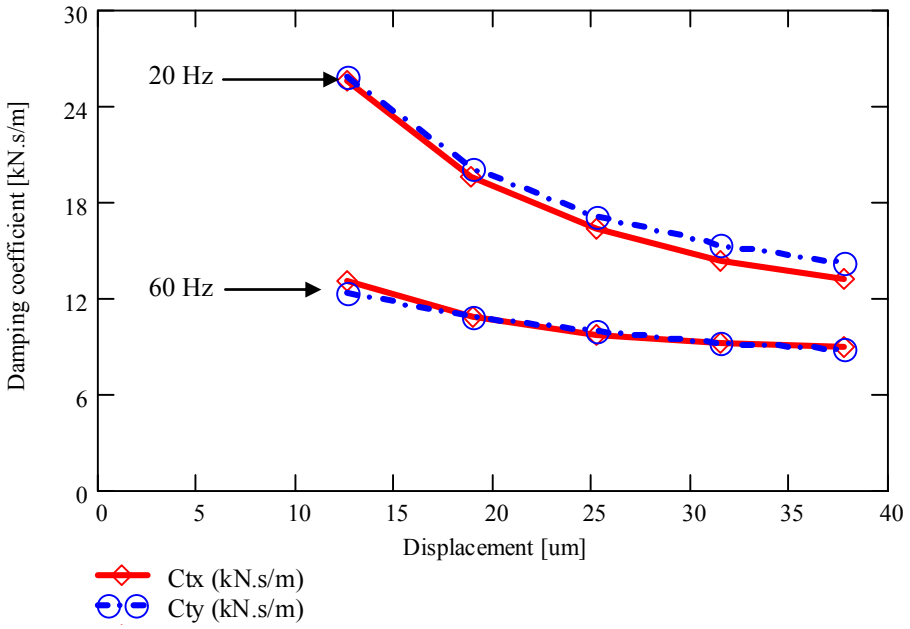

Figure 35 Identified system damping coefficients (C_{tx}, C_{ty}) versus displacement amplitude. (Excitation Frequency: 20 Hz and 60 Hz, Lubricated SFD)

Figures 36 and 37 depict the squeeze film damping coefficients (C_{xx}, C_{yy}) and model predictions versus displacement amplitude for the lowest and highest excitation frequencies, 20 Hz and 60 Hz, respectively. The short length, open ends bearing formula for damping coefficient is [2]

$$C_{rr} = \mu D\left(\frac{L}{c}\right)^3 \frac{\pi\left(1+2\varepsilon^2\right)}{2\left(1-\varepsilon^2\right)^2} \tag{16}$$

This formula considers a full film and is derived from small amplitude unidirectional motions about a static journal eccentricity ratio ($\varepsilon=e/c$). The test derived squeeze film damping coefficients (C_{xx}, C_{yy}) increase slightly with the amplitude of motion, though less pronouncedly as the model predictions. The test results at 60 Hz evidence invariant damping coefficients. For both frequencies, the simple model predictions are in good agreement with the identified coefficients. The average value of viscous damping is 6,000 Ns/m (34. 3 lb.s/in).

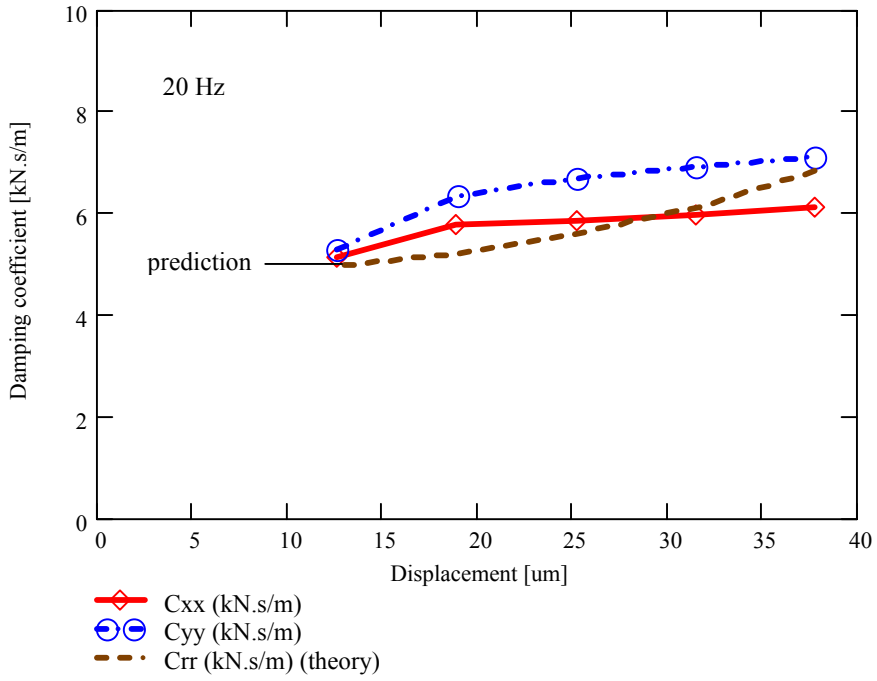

Figure 36 Squeeze film damping coefficients (C_{xx}, C_{yy}) versus displacement amplitude. (Excitation Frequency: 20 Hz, Lubricated SFD)

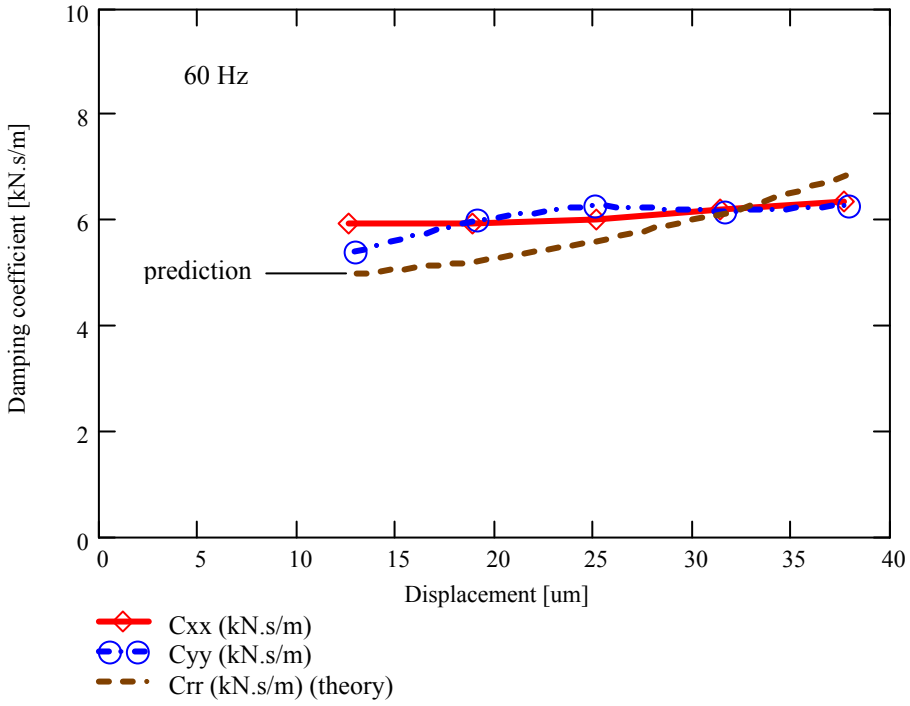

Figure 37 Squeeze film damping coefficients (C_{xx}, C_{yy}) versus displacement amplitude. (Excitation Frequency: 60 Hz, Lubricated SFD)

VII Conclusions and Recommendations

Exhaustive experiments were conducted to characterize the mechanical parameters of a SFD installed with an end mechanical seal. Structure stiffnesses are derived from static load tests without the seal in place. Periodic loads, single frequency, acting on the dry test system (no lubricant) aid to identify the dry friction force (26 N) at the mechanical seal contact surface.

Experimental test system damping and mass coefficients follow from unidirectional dynamic load excitations in the frequency range from 20 to 60 Hz. In the experiments, the load magnitudes vary to maintain prescribed amplitudes of motion. The parameter identification is carried in the frequency domain by building system transfer functions from the measured load and displacements. The test system damping combines the effects of dry-friction in the contact zone of the mechanical seal, the squeeze film damper, and a residual action from the structural supports. The system damping coefficients are larger at the lowest frequency and lowest amplitude of motion, denoting the paramount effect of dry friction in the mechanical seal. The estimated damping coefficients for the squeeze film alone are nearly independent of frequency, increasing slightly with the amplitude of dynamic motion.

The experimental results demonstrate the end seal effectively prevents air entrapment into the squeeze film land for the frequencies and amplitudes of motion tested. Further experimentation is planned to identify damping coefficients for elliptical motions, centered and off-centered. Future tests aim to vary the seal contact force and to replace the orifice discharge ports in order to simulate continued operation, wear and aging under extend periods of work, for example.

VIII References

[1] Rodriguez, L., Diaz, S., and San Andrés, L., 2000, "Sine Sweep Load Versus Impact Excitations and their Influence on the Identification of Damping in a Bubbly Oil Squeeze Film Damper," TRC report, TRC-SFD-3-00, May.

[2] Zeidan, F.Y., San Andrés, L., and Vance, J. M., 1996, "Design and Application of Squeeze Film Dampers in Rotating Machinery," Proceedings of the 25th Turbomachinery Simposium, Houston, TX, pp.169-188.

[3] Diaz, S., and San Andrés, L., 2000,"Orbit-Based Identification of Damping Coefficients of Off-centered Squeeze Film Damper including Support Flexibility," ASME Paper 2000-GT-0394.

[4] San Andrés, L., and Diaz, S., 2002, "Flow Visualization and Forces from a Squeeze Film Damper with Natural Air Entrapment," ASME Journal of Tribology, **125**(2), pp. 325-333

[5] Diaz, S., and San Andrés, L., 1999, "Reduction of the Dynamic Load Capacity in a Squeeze Film Damper Operating with a Bubbly Lubricant," ASME Journal of Gas Turbines and Power, **121,** pp. 703-709.

[6] Pietra, D., and Adiletta, G., 2002,"The Squeeze Film Damper over Four Decades of Investigations. Part I: Characteristics and Operating Features," The Shock and Vibration Digest, **34**(1), pp. 3-26.

[7] Pietra, D., and Adiletta, G., 2002,"The Squeeze Film Damper over Four Decades of Investigations. Part II: Rotordynamic Analyses with Rigid and Flexible Rotors," The Shock and Vibration Digest, **34**(2), pp. 97-126.

[8] San Andrés, L., and Vance, J., 1986, "Experimental Measurements of the Dynamic Pressure Distribution in a Squeeze-Film Bearing Damper Executing Circular-Centered Orbit," ASLE Transactions, **30**(3), pp. 373-383

[9] Roberts, J. B., Holmes, H., and Mason, T. J., 1986, "Estimation of Squeeze-Film Damping and Inertial Coefficients from Experimental Free-Decay Data," Proc. Instn Mech. Engrs, **200**(C2), pp 123-133

[10] Ellis, J., Roberts, J. B., and Hosseini, S. A., 1990, "The Complete Determination of Squeeze-Film Linear Dynamic Coefficients from Experimental Data," ASME Journal of Tribology, **112**, pp. 712-724

[11] Levesley, M., and Holmes, R., 1996, "The Effect of Oil Supply and Sealing Arrangements on the Performance of Squeeze-Film Dampers: an Experimental Study," Journal of Engineering Tribology: part J, **210**, pp. 221-232.

[12] De Santiago, O., and L. San Andrés, "Imbalance Response and Damping Force

Coefficients of a Rotor Supported on End Sealed Integral Squeeze Film Dampers," ASME Paper 99-GT-203

[13] Diaz, S., and San Andrés, L., "A Method for Identification of Bearing Force Coefficients and Its Application to a Squeeze Film Damper with a Bubbly Lubricant," STLE Tribology Transactions, Vol. 42 (4), pp. 739-746, 1999.

[14] San Andrés, L., and De Santiago, O., 2004, "Forced Response of a Squeeze Film Damper and Identification of Force Coefficients from Large Orbital Motions," ASME Journal of Tribology, **126**(2), pp. 292-300

[15] Delgado, A., and San Andrés, L., 2004, "Sealed end Squeeze Film Damper: Test rig Description and Identification of Structural Parameters," TRC report, TRC-SFD-1-04, May.

[16] Diaz, S., 2000, " CCO Data adquisition," LabView® virtual instrument. Texas A&M University, Tribology Group.

[17] Ginsberg, J. H., 2001, "Mechanical and Structural Vibrations," *John Wiley & Sons, Inc*., NY, pp. 135-139

[18] Pinkus, O., and Sternlight, B., 1961, *Theory of Hydrodynamic Lubrication,* McGraw-Hill Book Company Inc. , New York. pp. 34-35

[19] Delgado, A., San Andrés, 2005, "Identification of Structural Stiffness and Damping Coefficients of a Shoed Brush Seal," ASME Paper DETC 2005-84159, ASME IDETC/CIE Conference, Long Beach, CA, September

[20] Coleman, H. W., and Steele, G. W., 1988, *Experimentation and Uncertainty Analysis for Engineers,* JOHN WILEY & SONS, New York.

Appendix A Calibration of Eddy current sensors

This section describes the results and procedure followed for calibrating the eddy current sensors employed in the identification of the test rig structural parameters.

The calibration of the eddy current sensors was performed in situ (i.e. eddy current sensors attached to the rig). Two dial gauge (± 0.0001) with magnetic bases, located in the *X* and *Y* direction, made it possible to measure the actual displacement of the bearing housing. An ad-hoc device attached to the lower base of the test rig (as shown in Figure A 1) served to induce a steady displacement of the SFD housing. The calibration includes deflections in both directions of *X* and *Y*. Table A1 presents the gain of the eddy current sensors estimated from a linear regression of the calibration results shown in Figure A 2.

Table A1 Eddy current sensors gain estimated from calibration tests.

	X_1	X_2	Y_1	Y_2
Gain[mV/mils]	202	195	204	N/A
R^2	0.99	0.99	0.99	N/A
Serial #	H-108912	H-108877	H-108913	H-108914

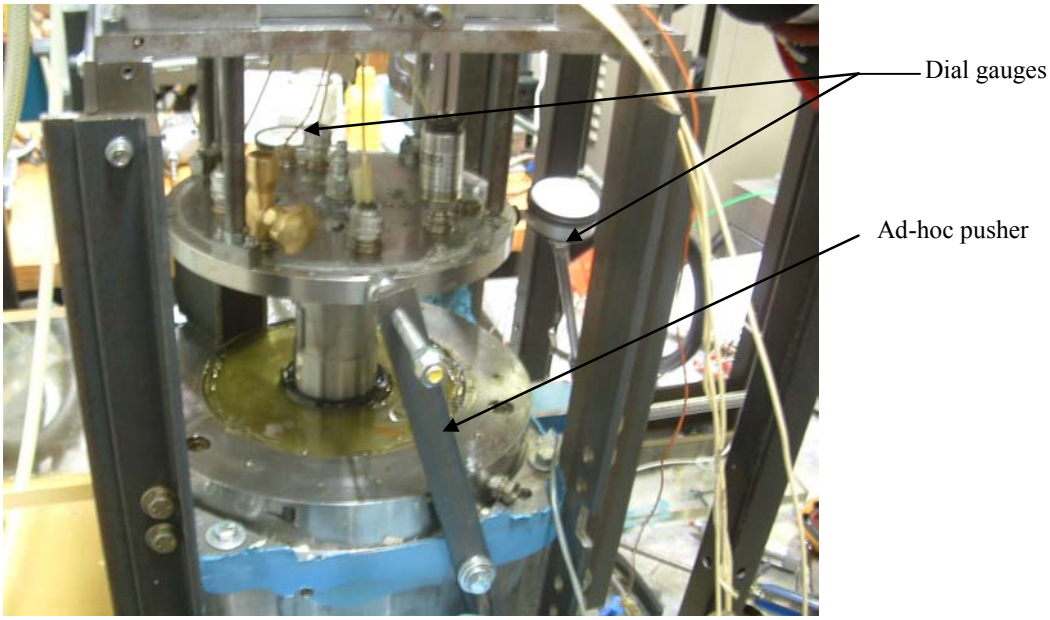

Figure A 1 Picture of VTR set up for calibrating eddy current sensors

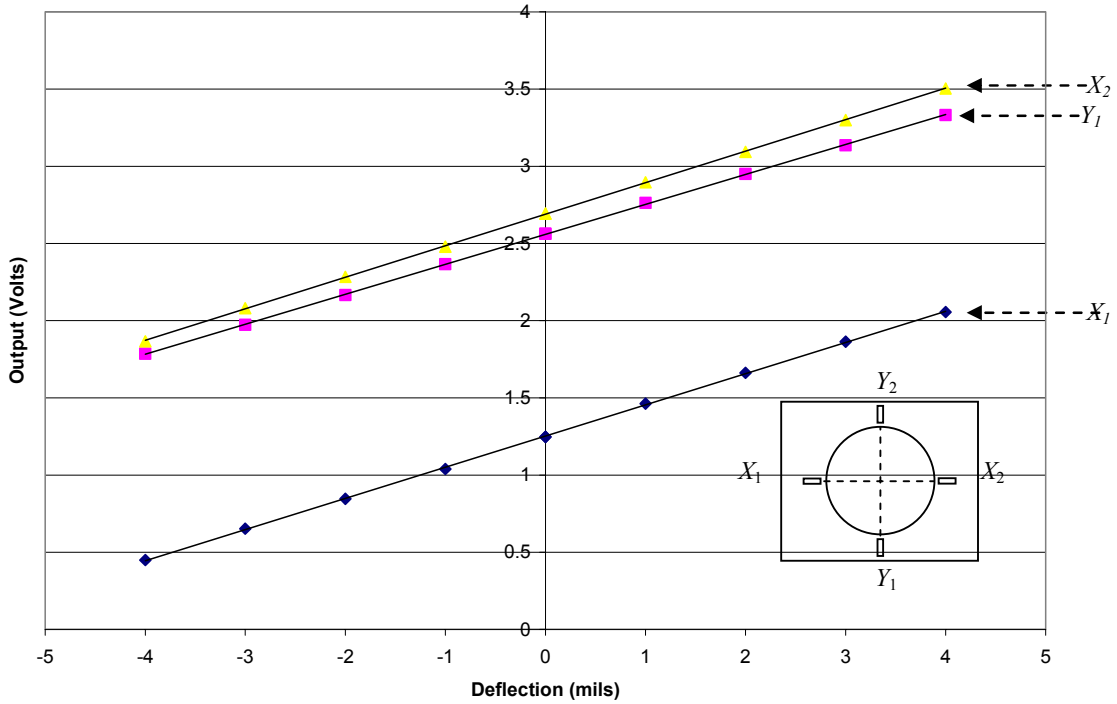

Figure A 2 Voltage output of eddy current sensors vs. displacement of SFD bearing. (Calibration test)

Appendix B Uncertainty analysis of test data

This section is dedicated to asses the uncertainty associated with the results reported in previous sections. The analysis contemplates the estimation of the error of each individual measurement, as well as the error propagation associated with parameters that are function of other variables.

B.1 Eddy current sensor calibration

The calibration of the proximity sensor (Appendix A) included readings from a displacement gauge ($U_d = \pm 0.0001$") and a voltmeter ($U_v = \pm\ 0.001\ V$). The uncertainty at each point is normally given by the precision and bias error of each instrument. However, for this calibration process, the uncertainty of each point (U_d, U_v) does not include the bias error of each instrument. Recall that the bias error is the fixed, systematic, or constant component of total error [20]. Thus, the calculation of the proximity sensor gains is not affected by the bias error, considering that the calculation of such gain is based on the relative value between each measurement (i.e. slope). On the other hand, the standard error of an estimate (*SEE*) can be used to obtain the goodness of the (least-squares) line that best fits the collection of pairs (voltage, displacement). That is, the *SEE*, given in equation (B.1) below, represents the deviation of the curve fit ($y=ax+b$) from the data set. The term "*N-2*" in the denominator arises from the two degrees of freedom lost from the set of *N* data pairs (X_i, Y_i) when determining the curve constants, *a* and *b* (slope and axis intersection) [20].

$$SEE = \left(\frac{\sum_{i=1}^{N} [Y_i - (aXi + b)]^2}{N - 2} \right)^{1/2} \tag{B.1}$$

The proximity sensor gain, given by the slope (*a*) of the curve fit, also follows the relationship

$$G = \frac{\Delta D}{\Delta V_{fit}} \tag{B.2}$$

with ΔD as the displacement variation and ΔV_{fit} as the voltage variation given by the linear fit.

The general equation used for calculating the uncertainty of parameters that are calculated from direct relations (i.e. $r=f(x_1,x_2,..x_n)$) is defined as [18]

$$U_r = \sqrt{\left(\frac{\partial r}{\partial x_1}U_{x_1}\right)^2 + \left(\frac{\partial r}{\partial x_2}U_{x_2}\right)^2 + ... + \left(\frac{\partial r}{\partial x_n}U_{x_n}\right)^2} \tag{B.3}$$

Then, from Equation B.3 the uncertainty of expression B.2 is

$$\left(\frac{U_G}{G}\right)^2 = \left(\frac{\partial G}{\partial D}\frac{U_D}{G}\right)^2 + \left(\frac{\partial G}{\partial V_{fit}}\frac{U_{V_{fit}}}{G}\right)^2 = \left(\frac{1}{\Delta D}U_D\right)^2 + \left(\frac{1}{\Delta V_{fit}}U_{V_{fit}}\right)^2 \tag{B.4}$$

where ΔD and ΔV_{fit} are given by the range of experimental values and $U_{V_{fit}}$ is calculated combining the voltmeter uncertainty (U_v) and the uncertainty of the curve fit given by the B.1 as

$$U_{V_{fit}} = \sqrt{\left(U_{fit}\right)^2 + \left(U_V\right)^2} \tag{B.5}$$

B.2 Parameter Identification

B.2.1 Static tests

The procedure to estimate uncertainty of the stiffness resulting from static test is similar to the one followed in the calibration of the proximity sensor. In this case, since each data pair (displacement, force) is the average from three different tests, the uncertainty of each point (in the displacement axis) of the force vs. displacement data collection is given by the combination of the instrument uncertainty (i.e. voltimeter) and the error incurred from averaging the three test, which is given by

$$U_{avg} = tS_{\bar{x}} \quad \text{t=4.303}, \qquad S_{\bar{x}} = S_x/\sqrt{N} \qquad ; \; S_x = \left[\frac{1}{N-1}\sum_{i=0}^{N}\left(X_i - \bar{X}\right)^2\right]^{1/2} \tag{B.6}$$

where $S_{\bar{x}}$ is the precision index of the mean value, S_x is the precision index; and, $\bar{X}$ and X_i represent the mean of the sample array and the individual samples, respectively. And t is the coefficient for 2 degrees of freedom (N-1) and a 95% confidence interval for a t-distribution of data points [18].

Subsequently, the uncertainty of the linear fit is given by B.1 and the uncertainty associated with the slope (stiffness coefficient) is defined as

$$\left(\frac{U_K}{K}\right)^2 = \left(\frac{1}{\Delta F}U_F\right)^2 + \left(\frac{1}{\Delta D_{fit}}U_{D_{fit}}\right)^2 + \left(\frac{1}{G}U_G\right)^2 \tag{B.7}$$

where

$$K = \frac{G}{V}F \tag{B.8}$$

B.2.2 Impact tests

For this case the uncertainty in the stiffness and mass coefficients is given by the uncertainty associated with the measurements of displacement and force (i.e. instrumentation uncertainty) and the error from the transfer function fit.

$$H(\omega) = \frac{1}{\left[\left(K^2 - M\omega^2\right)^2 + (C\omega)^2\right]^{1/2}} \tag{B.9}$$

This assumption is valid for stiffness and mass coefficient only, regarding that the curve fit matches the measured flexibility (i.e. displacement/ force) at $\omega \rightarrow 0$ (±4%), and that the stiffness and the mass given by the numerical fit follow from the expressions

$$H_{fit}(0) = \frac{1}{K}, \quad M = \frac{K}{\omega_n^2} \tag{B.10}$$

where the uncertainty of the natural frequency ω_n is given by the window resolution used in the dynamic frequency analyzer (400 Hz/400 lines= ± 1Hz resolution).

Therefore, the uncertainties of the stiffness and mass are

$$\frac{U_K}{K} = \frac{U_{H_{fit}}}{H(0)}, \quad \left(\frac{U_M}{M}\right)^2 = \left(\frac{U_K}{K}\right)^2 + \left(\frac{2U_K}{\omega_n}\right)^2 \tag{B.11}$$

where

$$\left(\frac{U_{H_{fit}}}{H_{fit}}\right)^2 = \left(\frac{U_F}{F}\right)^2 + \left(\frac{U_D}{D}\right)^2 + \left(1 - \frac{H}{H_{fit}}\right)^2$$

and

$$\left(\frac{U_F}{F}\right) = 0.01 \text{ (1\% linearity)}, \quad \left(\frac{U_D}{D}\right)^2 = \left(\frac{0.0008}{.03019}\right) = 7.84x10^{-4}$$

B.3 Flow Measurements

The flow meter is rated for flows of .3 to 3 GPM, and is field calibrated to ensure greater accuracy. The calibration procedure requires a container calibrated in one gallon increments from one to five. The container is calibrated by weighing water to estimate its volume as

$$gal._{h_2o} = Mass * \left(\frac{1}{\rho h_2 0} \right) * \left(\frac{1}{Cp} \right) \tag{B.12}$$

where mass as the liquid mass, ρ the density of water at 21 ^{0}C and Cp a conversion factor conversion factor (0.13368 ft^3/gal. h20)

The uncertainty of Eq. B.1 is related to the dynamometer used to weight the water and is given by the expression [20]

$$Ucalib. = \left[\left(\frac{\partial gal.}{\partial Mass} * Umass \right)^2 \right]^{1/2} \tag{B.13}$$

The uncertainty of the calibration of the container is 0.03 gallons.

Field calibration of the flow meter involves reading the amount of liquid in the container and inputting the data into the flow meter. The level of liquid in the calibration container can be read at an accuracy of 1/16" from the actual gallon mark. The combined error of the calibration is 0.04 Gal. The bias error of the flow meter is given by the manufacturer as %1.5 of the measured value.

Pressure is measured using Omega® PX-215 pressure sensors. The sensors operate on a process current from 4 to 20mA. This current is read by a digital ammeter before entering the Omega® display. The current output of the pressure sensors was calibrated to pressures using an Ashcroft portable gauge tester. The current measured is converted to pressure using equation

$$P = k * ip + C_2 \tag{B.14}$$

where k is the pressure sensor calibration constant, ip the measured current (mA) and C_2 intercept of pressure calibration curve

The equation for the pressure sensor calibration constant is given by

The uncertainties used in this analysis were the uncertainty of the Ashcroft portable tester and the digital ammeters. The uncertainty values for the pressure sensors at the

inlet and recirculation annals are calculated at 5 psig. The uncertainty of the calibration (Eq. B.3) is given by [20]

$$Uk = \left[\left(\frac{\partial k}{\partial P} * UP_{calib.} \right)^2 + \left(\frac{\partial k}{\partial ip} * Uip \right)^2 \right]^{1/2} \tag{B.15}$$

Combining the uncertainty of the calibration and the uncertainty of the ammeter reading yields the uncertainty of the pressure measurement

$$Up = \left[\left(\frac{\partial P}{\partial k} * Uk \right)^2 + \left(\frac{\partial P}{\partial ip} * Uip \right)^2 \right]^{1/2} \tag{B.16}$$

The uncertainty of the inlet pressure reading is 0.182 psig. The uncertainty of the pressure readings at the recirculation annulus is 0.177 psig.

For the flow measurements the precision index for each sample is calculated as [20]

$$S_X = \left[\frac{1}{N-1} \sum_{i=1}^{N} \left(X_i - \overline{X} \right)^2 \right]^{1/2} \tag{B.17}$$

and the precision index of the mean is

$$S_{\overline{X}} = S_X / \sqrt{N} \tag{B.18}$$

where N is the number of samples , X is the sample values and $\overline{X}$ is the mean value of the sample population. The t value for %95 confidence with three samples is 4.3. The precision error is [20]

$$P_{\overline{X}} = tS_{\overline{X}} \tag{B.19}$$

The bias error is a combination of the calibration errors and the manufacturer given %1.5 bias error.

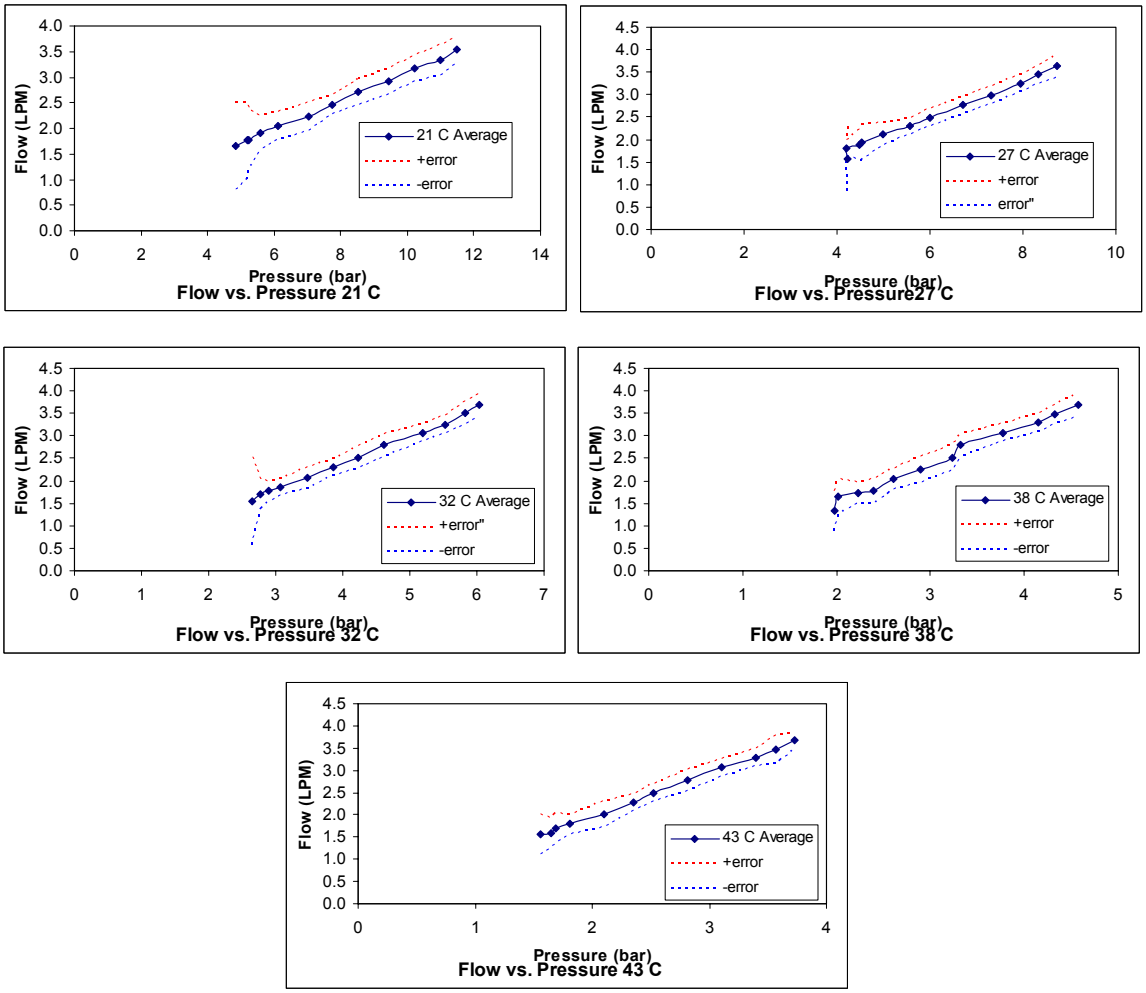

Figure B 1 Lubricant flow through SFD vs. inlet pressure. (average from three sets of tests)

Appendix C Orbits at 30 Hz, 40 Hz, 50 Hz, 90 Hz from dynamic tests (SFD not lubricated)

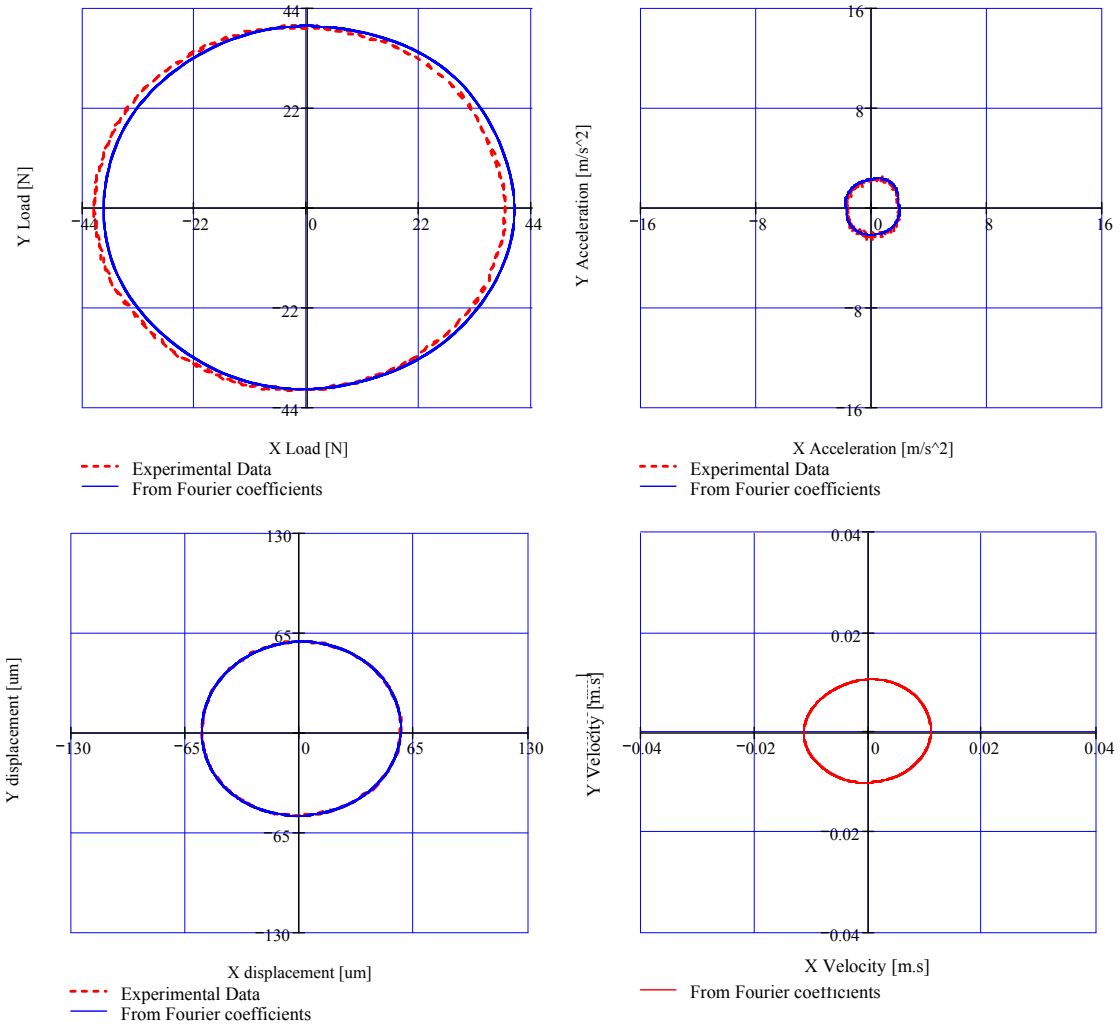

Figure C 1 Excitation and response orbits from experimental data and Fourier coefficients. Velocity orbit built from Fourier coefficients of the displacement response. (40 N, 30 Hz)

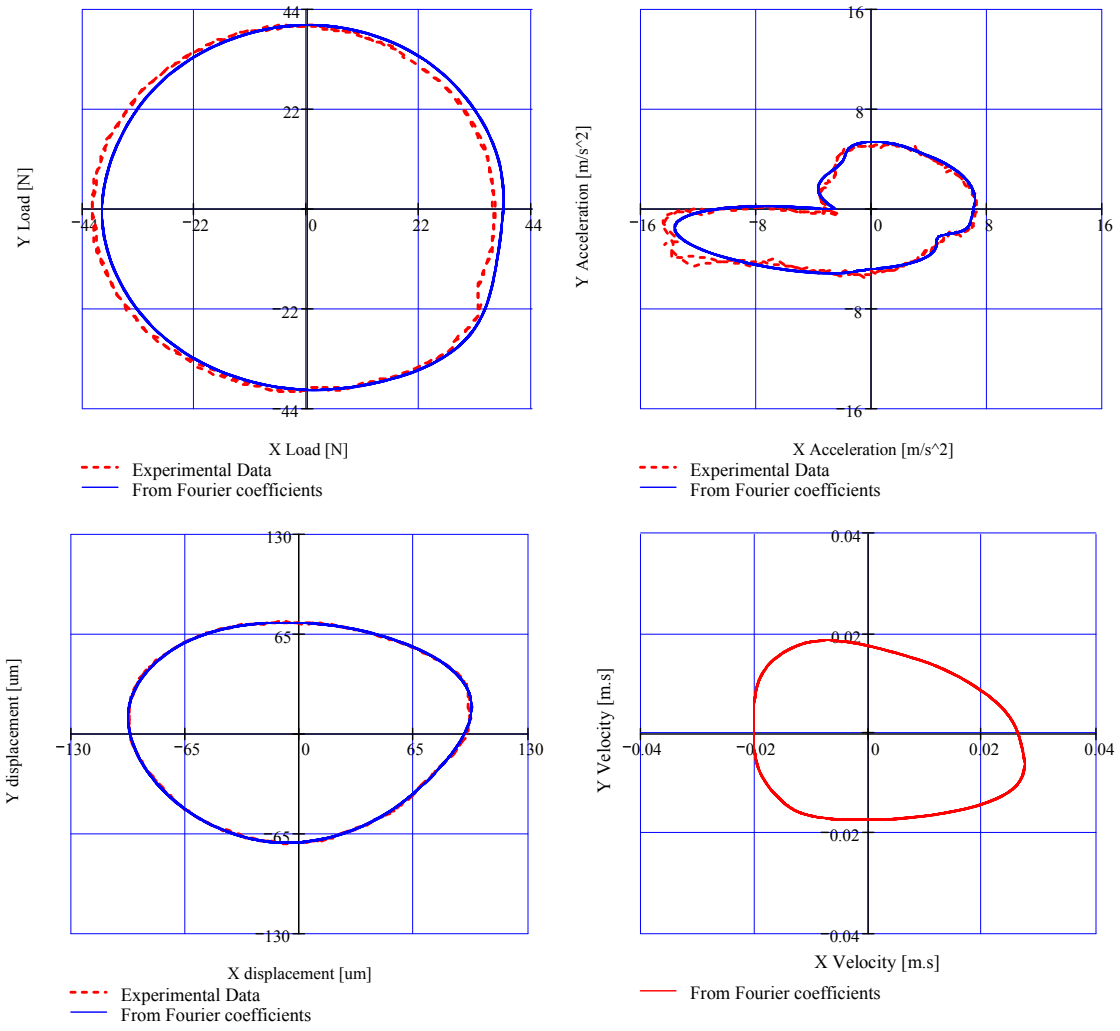

Figure C 2 Excitation and response orbits from experimental data and Fourier coefficients. Velocity orbit built from Fourier coefficients of the displacement response. (40 N, 40 Hz)

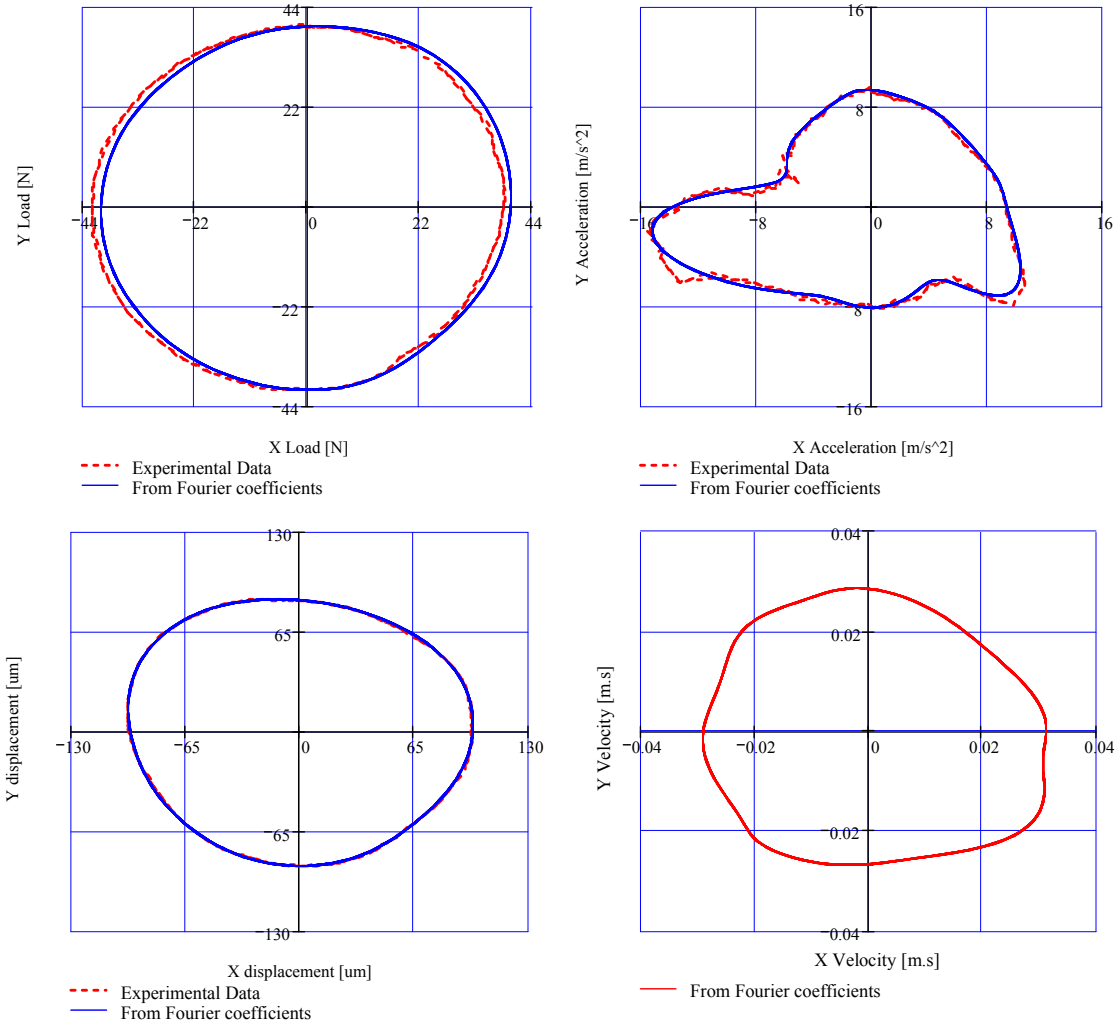

Figure C 3 Excitation and response orbits from experimental data and Fourier coefficients. Velocity orbit built from Fourier coefficients of the displacement response. (40 N, 50 Hz)

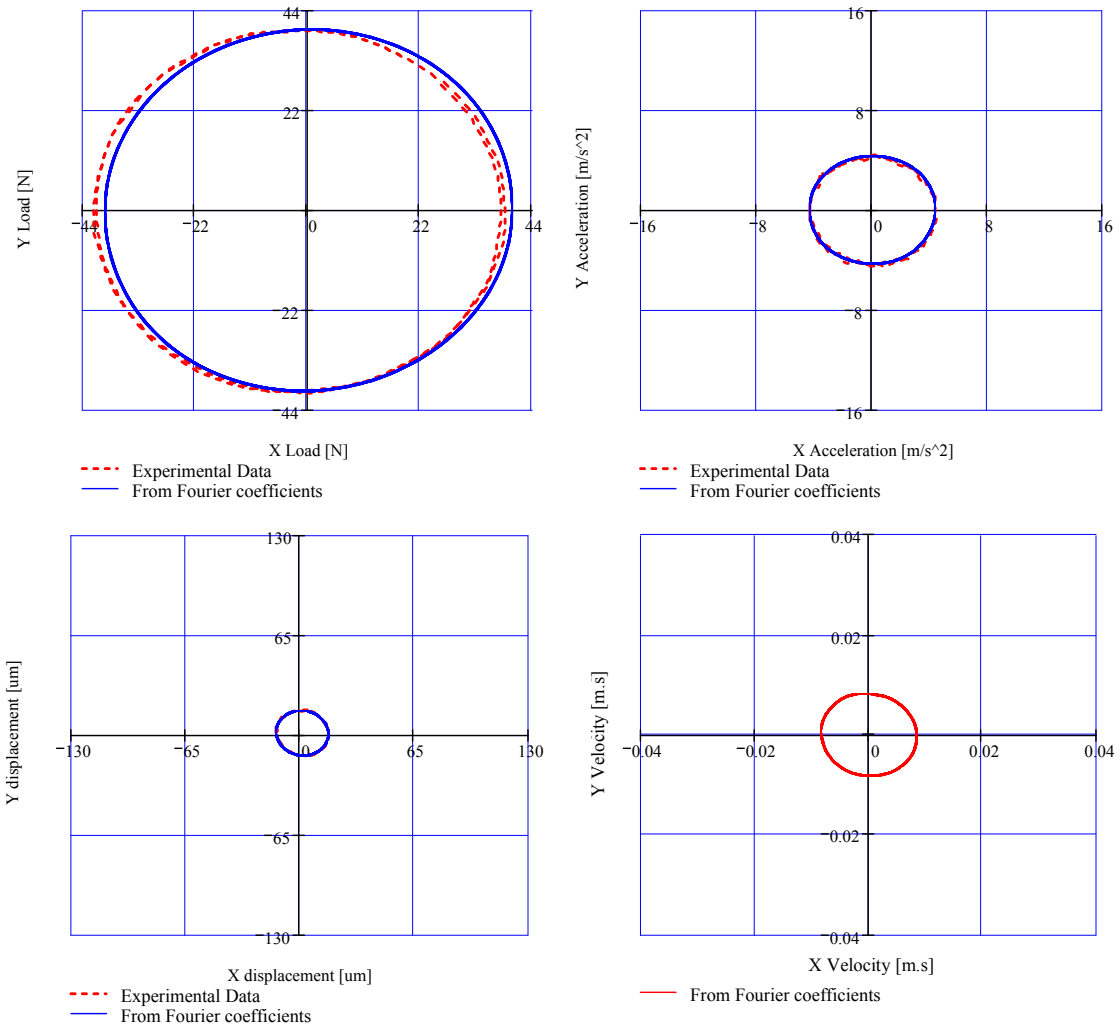

Figure C 4 Excitation and response orbits from experimental data and Fourier coefficients. Velocity orbit built from Fourier coefficients of the displacement response. (40 N, 90 Hz)

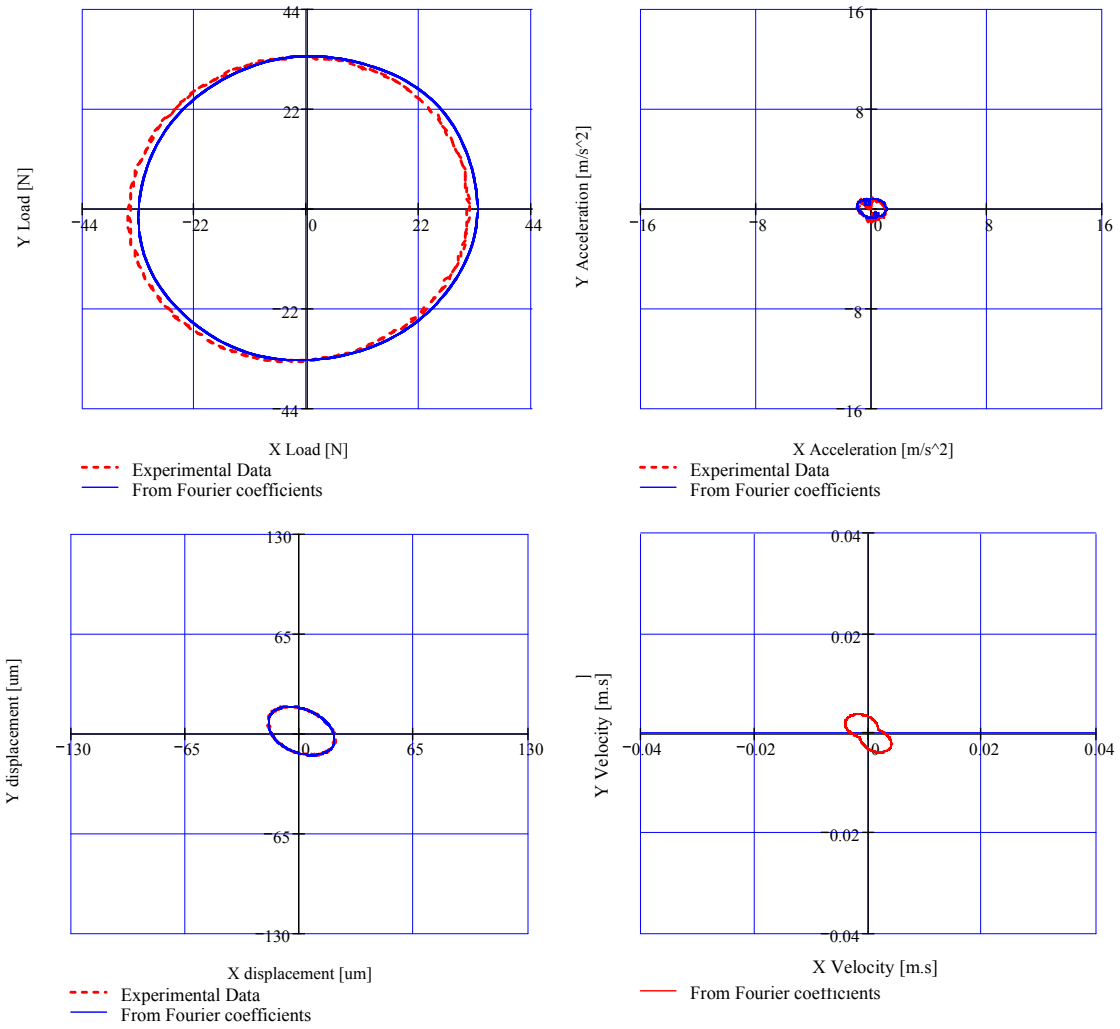

Figure C 5 Excitation and response orbits from experimental data and Fourier coefficients. Velocity orbit built from Fourier coefficients of the displacement response. (33 N, 30 Hz)

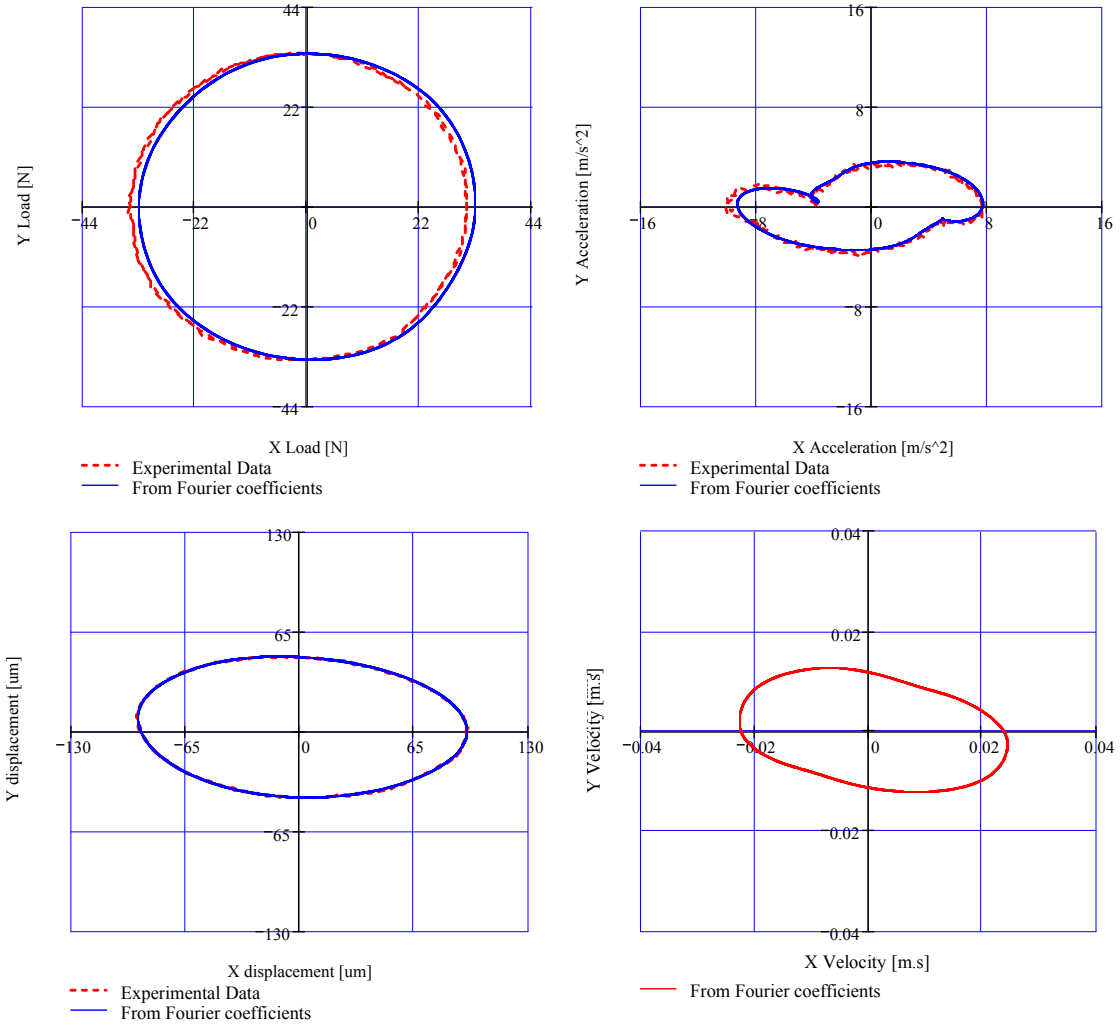

Figure C 6 Excitation and response orbits from experimental data and Fourier coefficients. Velocity orbit built from Fourier coefficients of the displacement response. (33 N, 40 Hz)

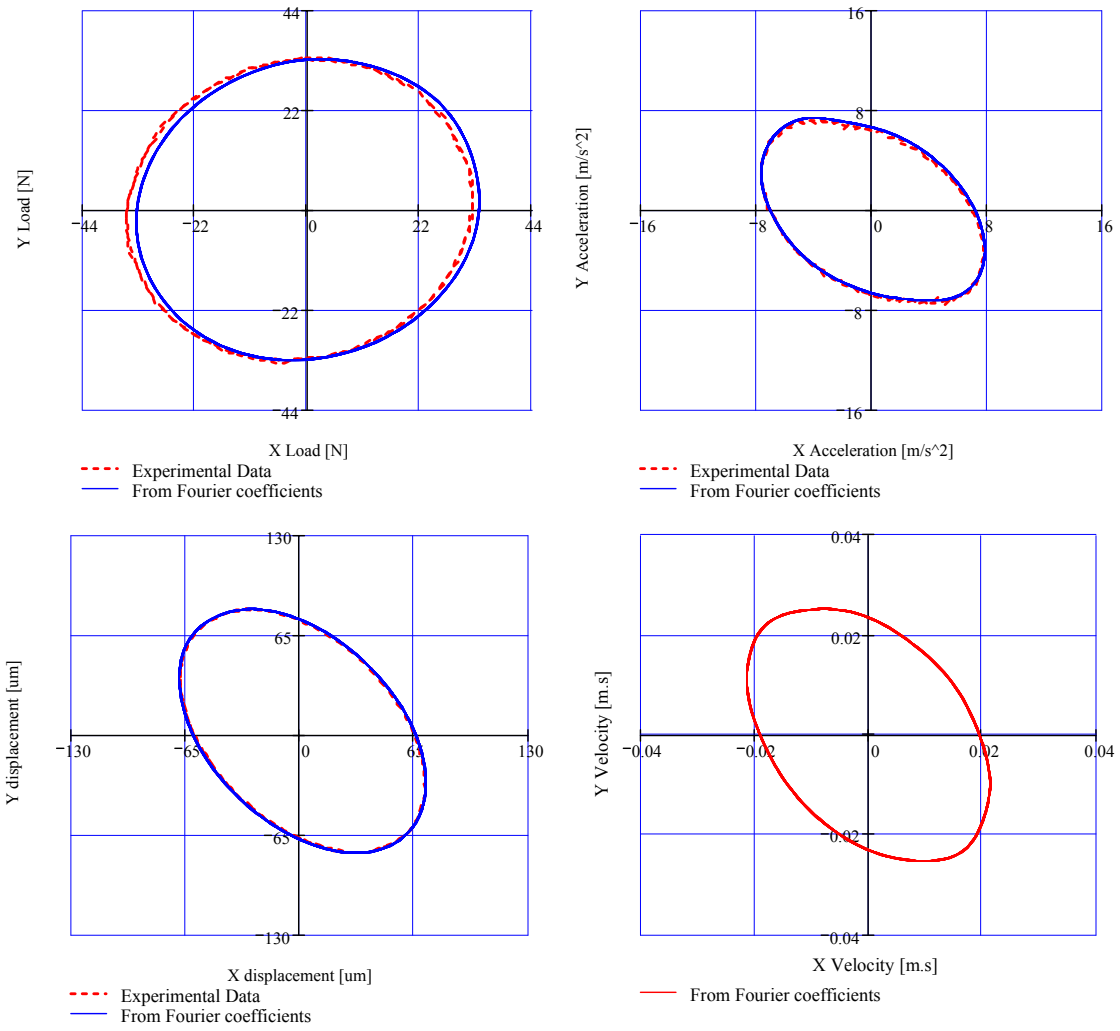

Figure C 7 Excitation and response orbits from experimental data and Fourier coefficients. Velocity orbit built from Fourier coefficients of the displacement response. (33 N, 50 Hz)

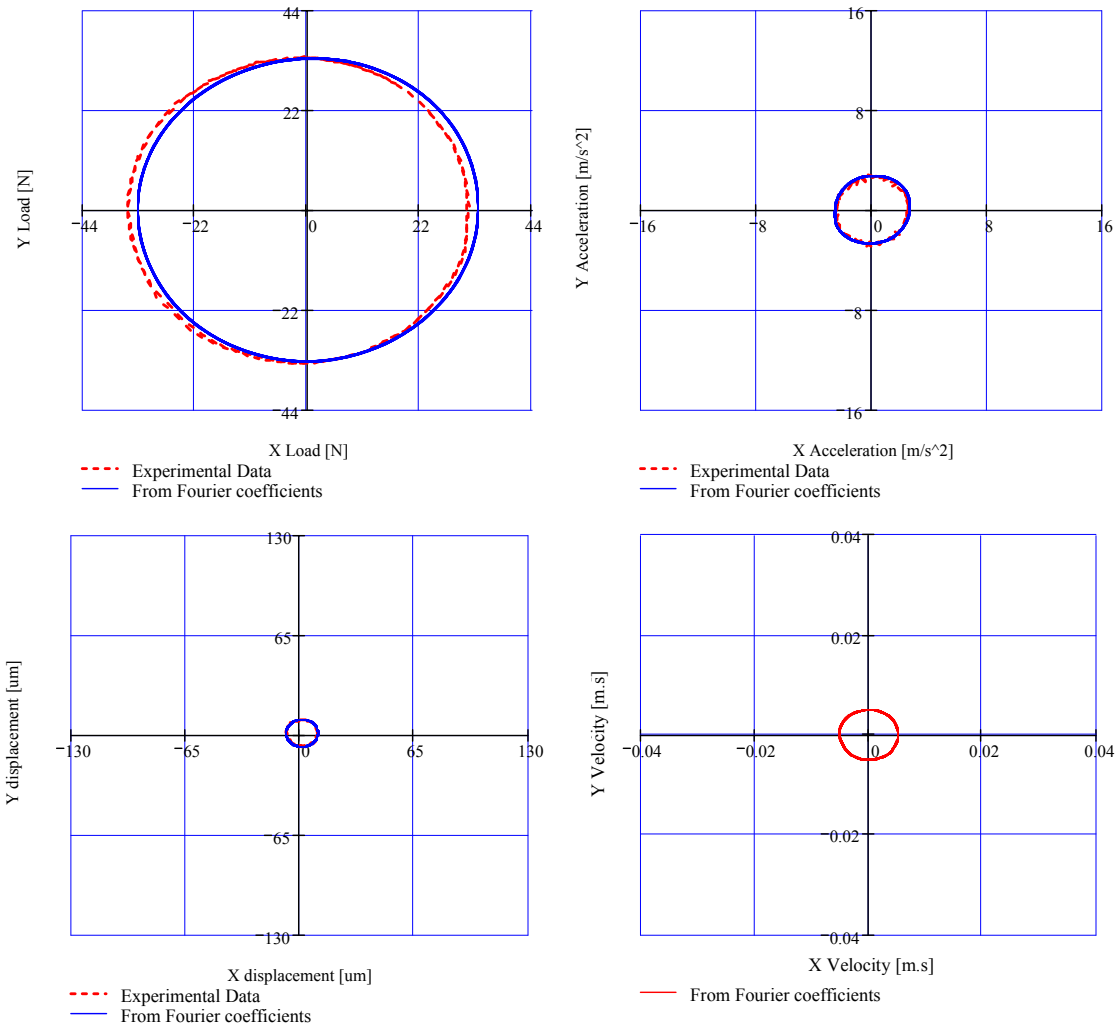

Figure C 8 Excitation and response orbits from experimental data and Fourier coefficients. Velocity orbit built from Fourier coefficients of the displacement response. (33 N, 90 Hz)

Appendix D Displacement Traces from unidirectional dynamic tests

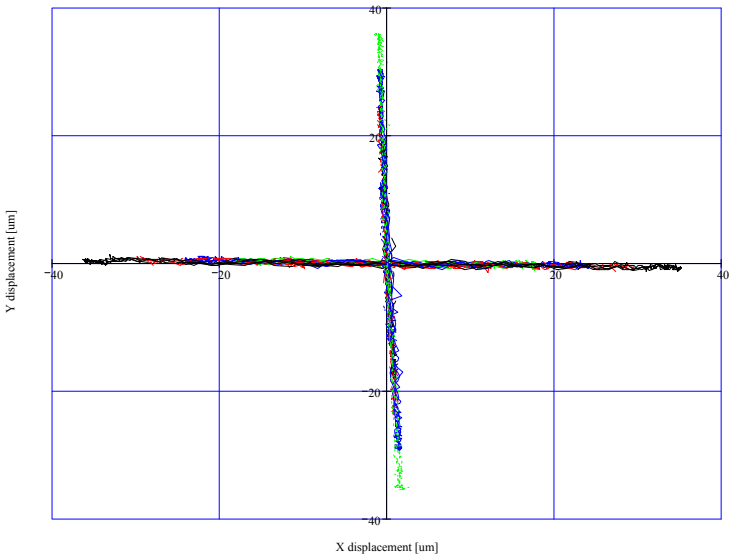

Figure D 1 Displacement trace in X and Y due to a unidirectional load in X and Y directions, respectively (20 Hz)

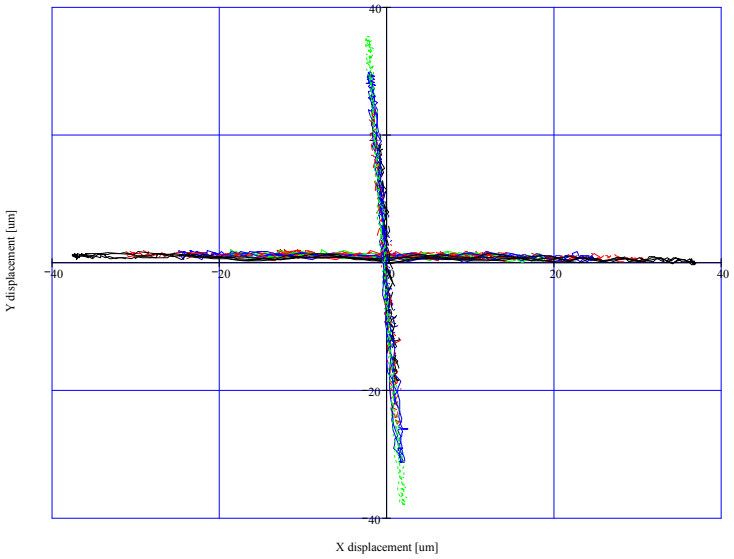

Figure D 2 Displacement trace in X and Y due to a unidirectional load in X and Y directions, respectively. (30 Hz)

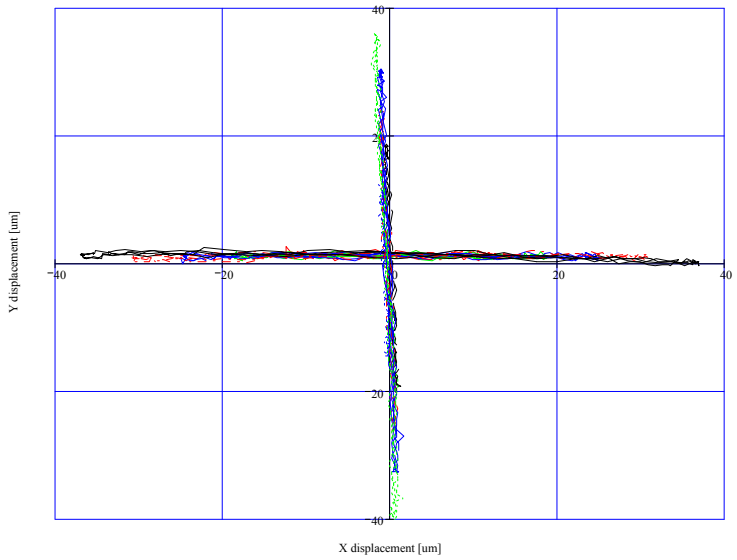

Figure D 3 Displacement trace in X and Y due to a unidirectional load in X and Y directions, respectively (40 Hz)

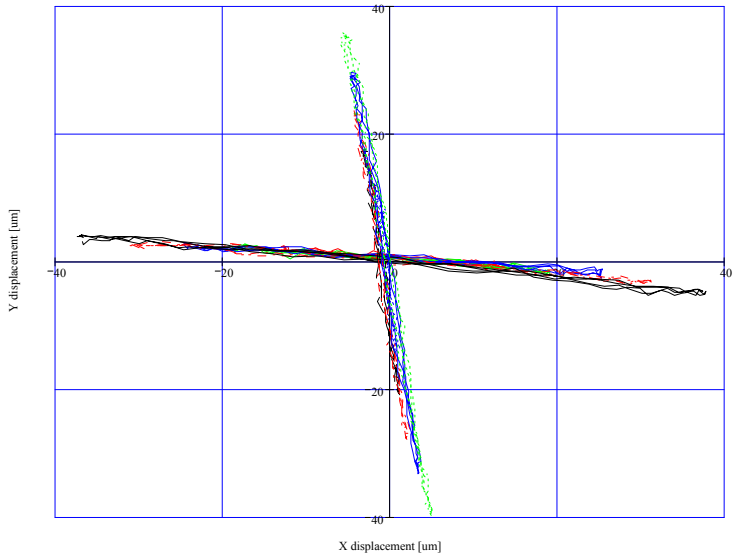

Figure D 4 Displacement trace in X and Y due to a unidirectional load in X and Y directions, respectively (50 Hz)

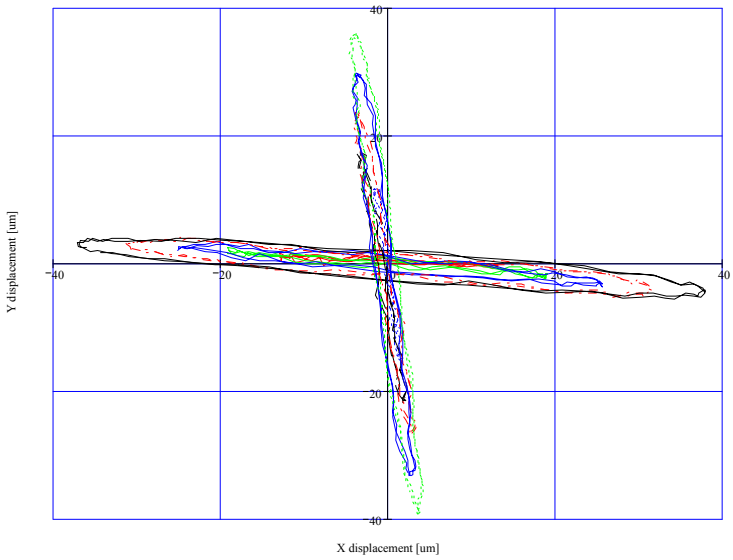

Figure D 5 Displacement trace in X and Y due to a unidirectional load in X and Y directions, respectively (60 Hz)

Appendix E Squeeze film added mass coefficients as a function of displacement amplitude

This appendix shows the added mass coefficient identified from the unidirectional periodic excitation load tests. The coefficients are extracted from system dynamic stiffness and are presented in Table F 1.

Table F 1 Added mass coefficients and correlation factors

		Coefficient [kg]	Correlation (r^2)
13 μm	D_{xx}	6.8	0.92
	D_{yy}	3.2	0.79
19 μm	D_{xx}	8.4	0.98
	D_{yy}	5.2	0.87
25 μm	D_{xx}	8.9	0.92
	D_{yy}	6.2	0.98
32 μm	D_{xx}	9.1	0.99
	D_{yy}	7.7	0.96
38 μm	D_{xx}	9.4	0.98
	D_{yy}	8.1	0.96

Figure F1 depicts the identified added mass coefficients versus displacement amplitude. For motion amplitudes less than 32 μm, the correlation factor for the analytical fit is not good ($r^2 < 0.92$), and which makes the test results not reliable. Further testing is needed to asses the added mass coefficients at low amplitudes of motion.

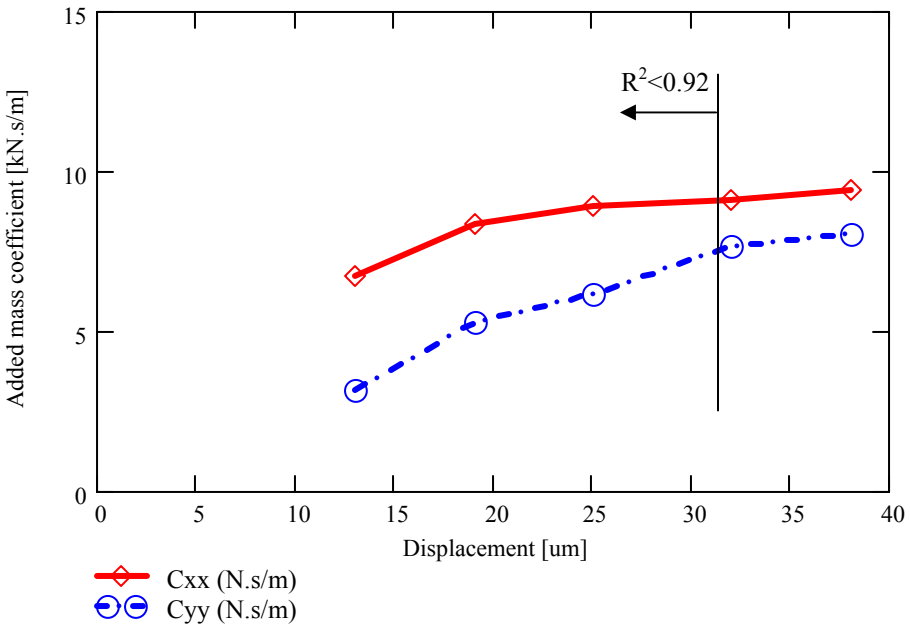

Figure F 1 Added mass coefficient versus displacement amplitude. (Identification range 20-60Hz)

Appendix F Identified squeeze film damping coefficients as function of displacement amplitude and frequency

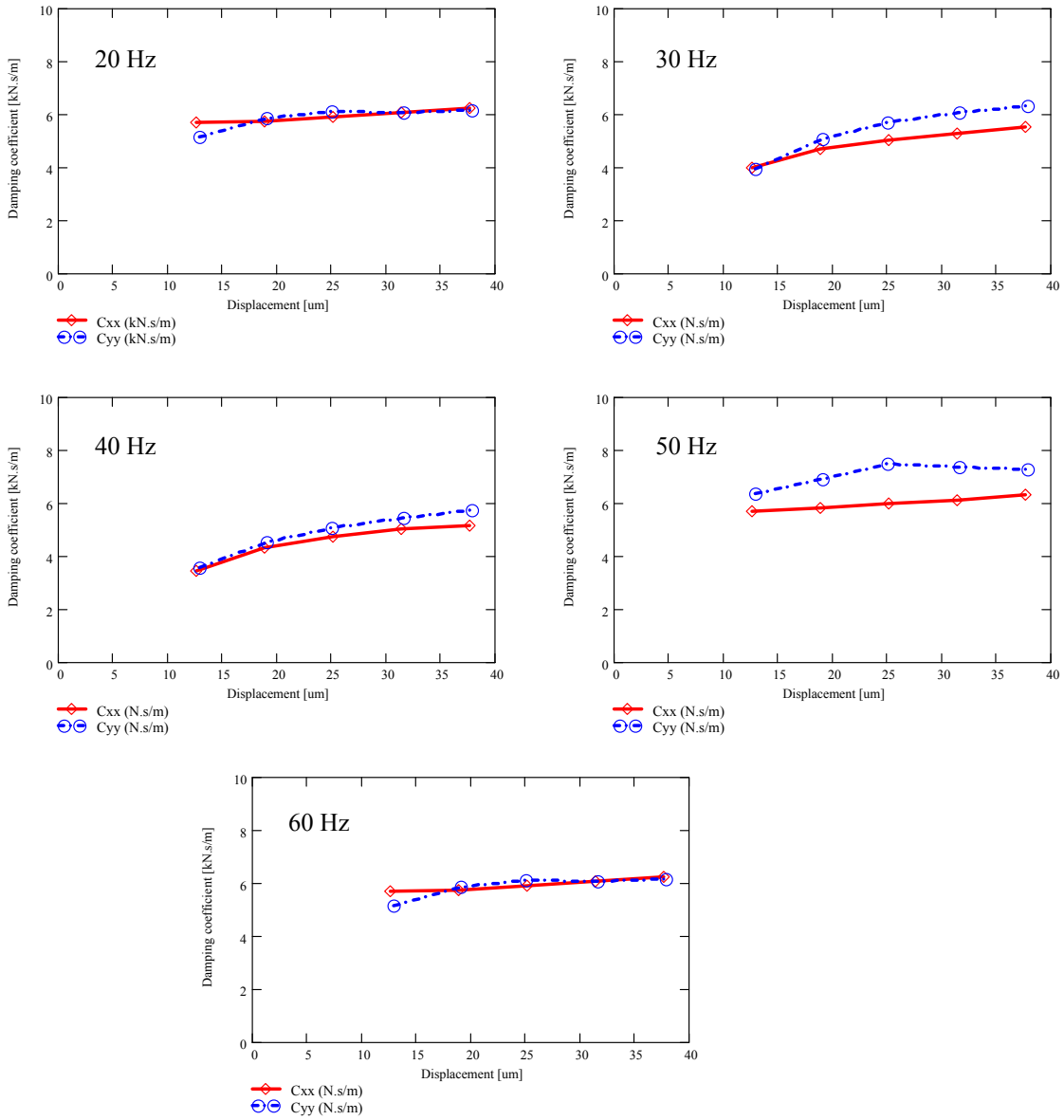

Figure E 1 Squeeze film damping coefficients vs. displacement amplitude for 5 excitation frequencies (20 Hz, 30 Hz, 40 Hz, 50 Hz, 60 Hz).

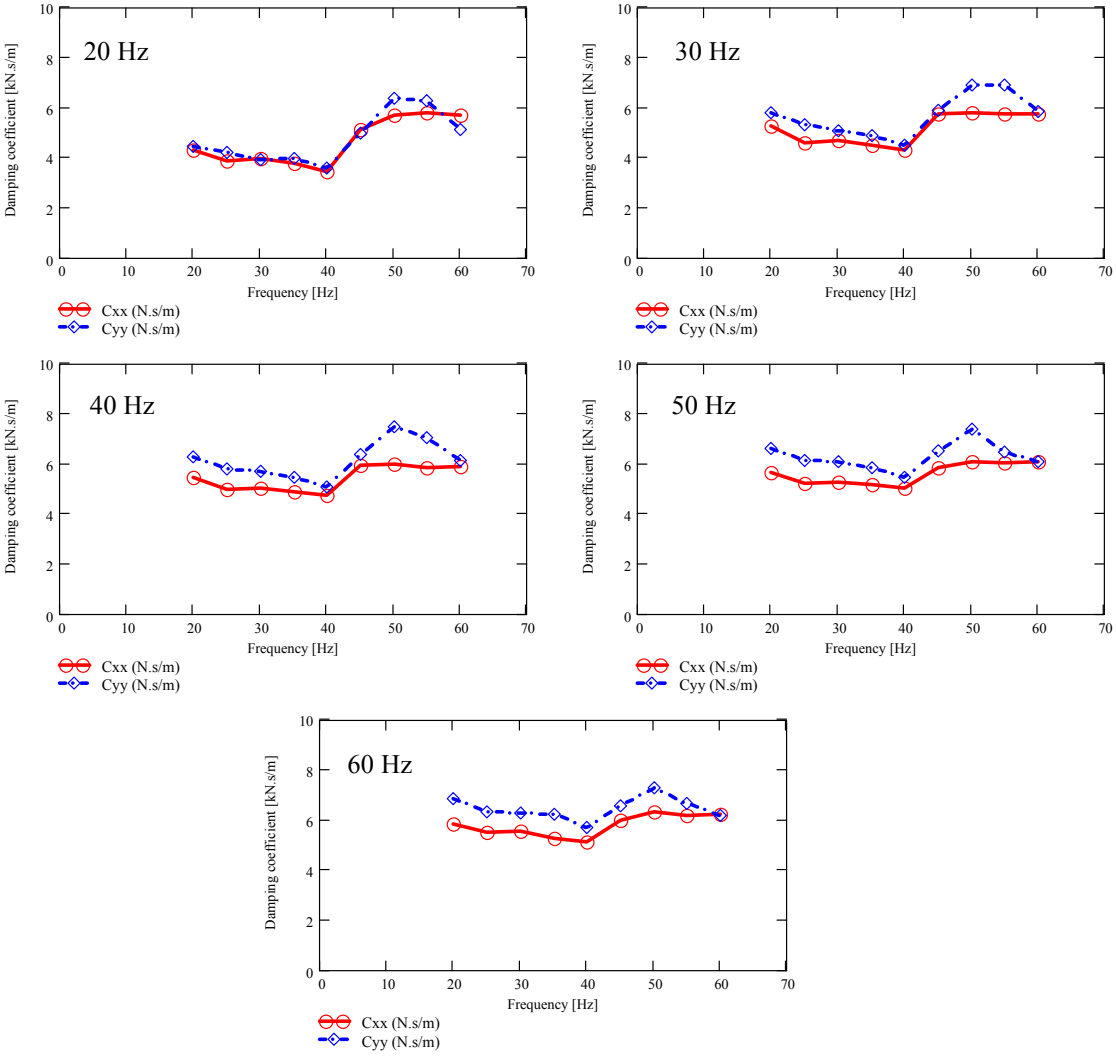

Figure E 2 Viscous damping coefficient vs. excitation frequency for 5 constant displacement amplitudes (13 μm, 19 μm, 25 μm, 32 μm, 38 μm).